JOURNAL OF GEOPHYSICAL RESEARCH, VOL. 114, A02201, doi:10.1029/2008JA013128, 2009

Relativistic-electron dropouts and recovery: A superposed epoch study of the magnetosphere and the solar wind

Joseph E. Borovsky[1] and Michael H. Denton[2]

Received 26 February 2008; revised 3 June 2008; accepted 28 October 2008; published 5 February 2009.

[1] During 124 high-speed-stream-driven storms from two solar cycles, a multispacecraft average of the 1.1–1.5 MeV electron flux measured at geosynchronous orbit is examined to study global dropouts of the flux. Solar wind and magnetospheric measurements are analyzed with a superposed epoch technique, with the superpositions triggered by storm-convection onset, by onset of the relativistic-electron dropouts, and by recovery of the dropouts. It is found that the onset of dropout occurs after the passage of the IMF sector reversal prior to the passage of the corotating interaction region (CIR) stream interface. The recovery from dropout commences during the passage of the compressed fast wind. Relativistic-electron-dropout onset is temporally associated with the onset of the superdense ion and electron plasma sheet, with the onset of the extra-hot ion and electron plasma sheet and with the formation of the plasmaspheric drainage plume. Dropout recovery is associated with the termination of the superdense plasma sheet and with a decay of the plasmaspheric drainage plume. When there is appreciable spatial overlap of the superdense ion plasma sheet with the drainage plume, dropouts occur, and when that overlap ends, dropouts recover. This points to pitch-angle scattering by electromagnetic ion-cyclotron (EMIC) waves as the primary cause of the relativistic-electron dropouts, with the waves residing in the lumpy drainage plumes driven by the superdense ion plasma sheet. The drainage plume is caused by enhanced magnetospheric convection associated with southward (GSM) magnetic field after the IMF sector reversal. The superdense plasma sheet has its origin in the compressed slow wind of the CIR.

Citation: Borovsky, J. E., and M. H. Denton (2009), Relativistic-electron dropouts and recovery: A superposed epoch study of the magnetosphere and the solar wind, *J. Geophys. Res.*, *114*, A02201, doi:10.1029/2008JA013128.

1. Introduction

[2] Relativistic-electron dropouts are an integral aspect of the behavior of the outer radiation belt during geomagnetic storms. Early in a storm, the outer-electron-radiation-belt fluxes rapidly decrease (dropout) and later the fluxes rapidly return (recovery) [cf. *Freeman*, 1964; *Nagai*, 1988; *Blake et al.*, 2001; *Onsager et al.*, 2002; *Green et al.*, 2004]. During the dropouts the relativistic-electron fluxes can decrease by decades [e.g., *Kim and Chan*, 1997; *Li et al.*, 1997], as can the relativistic-electron number densities [*Borovsky et al.*, 1998a; *Borovsky and Steinberg*, 2006]. At geosynchronous orbit dropouts begin at one location and spread in local time [*Onsager et al.*, 2002] and have durations of 13 ± 7 hours [*Borovsky and Steinberg*, 2006]. The cause of the dropouts is an outstanding issue for radiation-belt dynamics [*Friedel et al.*, 2002] and for high-speed-stream-driven storms [*Kavanagh and Denton*, 2007; *Denton et al.*, 2008].

[3] Some examples of relativistic-electron dropouts are shown in Figure 1 where relativistic-electron measurements from the spacecraft 1989–046 in geosynchronous orbit carrying the SOPA instrument [*Belian et al.*, 1992] are shown for 200 days in 1993–1994 when repeating high-speed-stream-driven storms were occurring. The top curve is the flux in the 1.1–1.5 MeV electron channel and the bottom curve is the number density of relativistic electrons determined with relativistic-Maxwellian fits to the measured 30-keV to 2-MeV electron fluxes [cf. *Cayton et al.*, 1989]. Relativistic-electron dropouts are marked in red for both curves. Note in Figure 1 that the relativistic-electron number densities tend to be higher after dropouts then before, whereas the relativistic-electron fluxes can be higher or lower (fluxes being a function of both the density and the temperature of the relativistic electrons).

[4] Relativistic-electron dropouts occur during the main phase of a storm, simultaneous with increases in Kp [*Nagai*, 1988] and with the sharp drops of Dst [*Nagai*, 1988; *Kim and Chan*, 1997; *Iles et al.*, 2002]. The relativistic-electron dropouts have been associated with the occurrence of the superdense plasma sheet [*Borovsky et al.*, 1998a; *Green et al.*, 2004] and with the occurrence of plasmaspheric drainage plumes [*Borovsky and Steinberg*, 2006]. In connection

[1]Space Science and Applications, Los Alamos National Laboratory, Los Alamos, New Mexico, USA.
[2]Department of Communication Systems, Lancaster University, Lancaster, UK.

0148-0227/09/2008JA013128$09.00

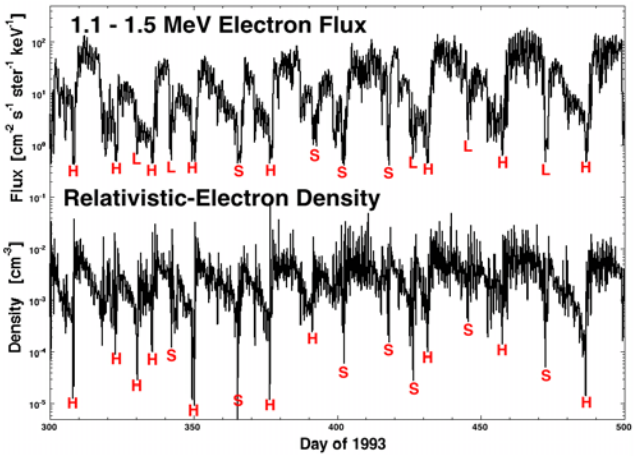

Figure 1. For 200 days in 1993–1994, the flux of 1.1–1.5 MeV electrons as measured by the SOPA instrument onboard 1989-046 is plotted (top curve) and the relativistic-electron number density determined by fits to the electron fluxes measured at all energies in the SOPA instrument onboard 1989–046 is plotted (bottom curve). Relativistic-electron dropouts are marked with the red letters. In the top curve, the letter indicates whether the flux was higher (H), similar (S), or lower (L) immediately after the dropout recovery than immediately before the dropout. In the bottom curve, the letter indicates whether the number density was higher (H), similar (S), or lower (L) immediately after the dropout recovery than immediately before the dropout.

with the solar wind, the relativistic-electron dropouts are associated with the onset of southward IMF [*Iles et al.*, 2002] and solar wind dynamic pressure increases [*Onsager et al.*, 2007].

[5] Relativistic-electron dropouts occur both for CME-driven storms [e.g., *Bortnik et al.*, 2006] and for high-speed-stream-driven storms [e.g., *Li et al.*, 1997]. High-speed-stream-driven storms [*Burlaga and Lepping*, 1977; *Tsurutani et al.*, 2006a, 2006b] are particularly interesting because of the robust outer-radiation-belt intensification over time in the days after recovery from dropout [e.g., *Paulikas and Blake*, 1976; *Reeves*, 1998; *Love et al.*, 2000; *Lam*, 2004; *Borovsky and Denton*, 2006] [see also *Rostoker et al.*, 1998; *Mathie and Mann*, 2000]. High-speed-stream-driven storms are also particularly amenable to study by superposed epoch methods [cf. *McPherron and Weygand*, 2006; *Denton et al.*, 2006; *Denton and Borovsky*, 2008a] because they have a repeating sequence of solar wind types that pass the Earth. T (cf. Figure 1 of *Richardson et al.* [1996]): fast wind, rarefaction, slow wind, onset of CIR, compressed slow wind (westward flow), sector reversal within the compressed slow wind, stream interface, compressed fast wind (eastward flow), end of CIR, and again fast wind, rarefaction, . . . This sequence can be seen in the sketch of a CIR in Figure 2 with the temporal track of the Earth through h the CIR shown in green. This repeating sequence is listed in the first column of Table 1 where the chronology of relativistic-electron dropouts will be meshed into the chronology of the solar wind and the magnetosphere.

[6] Note that the storm time relativistic-electron dropouts discussed in this report are not to be confused with the brief (~1/2 hour) energetic-particle dropouts seen in the nightside sector of geosynchronous orbit just prior to substorm particle-injection events and global sawtooth oscillations [cf. *Erickson and Winckler*, 1973; *Bogott and Mozer*, 1973; *Sauvaud and Winckler*, 1980] which are caused by local extreme stretching of the magnetic field at geosynchronous orbit [e.g., *Baker and McPherron*, 1990; *Thomsen et al.*, 1994; *Sauvaud et al.*, 1996].

[7] In this report we will use superposed epoch analysis of 124 high-speed-stream-driven storms to study relativistic-electron dropouts and their association with solar wind and magnetospheric processes. We aim to find out what the

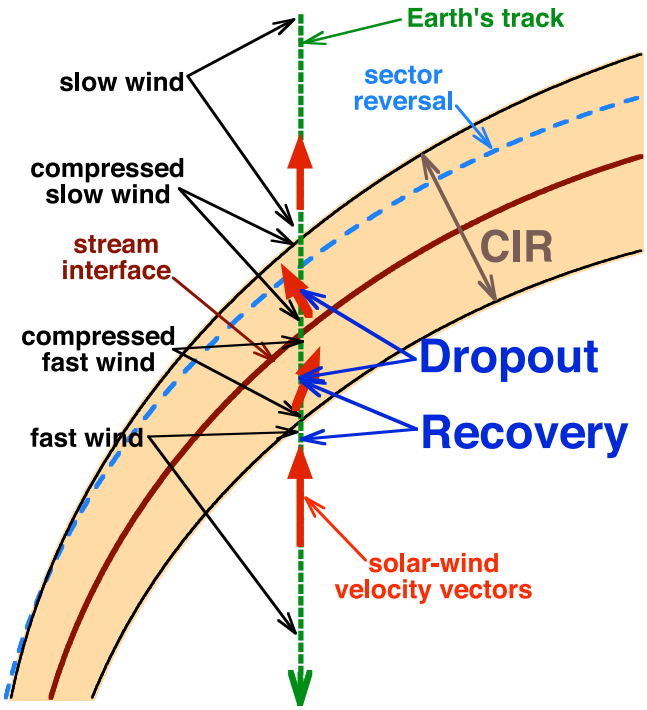

Figure 2. Looking down onto the ecliptic plane from above, a CIR near Earth's orbit is sketched. The Sun is off the bottom of the figure. The CIR is shaded in tan, and the Earth's track through the CIR is depicted as the green dashed line. In the reference frame of this sketch, the Earth moves downward with time. The solar wind flow direction is shown with red arrows. At first, the Earth is in the slow wind ahead of the CIR. As the Earth enters the CIR, it enters into compressed slow wind with a flow deflection to the left. When the Earth crosses the stream interface (dark red), it exits the compressed slow wind and enters the compressed fast wind and the flow deflection switches from left to right. When the Earth exits the CIR, it exits into fast wind with no flow deflection. Typically, ahead of the stream interface, there is a magnetic-field sector reversal (light-blue dashed curve) where the field switches from inward to outward or from outward to inward. In dark blue, the positions of the Earth on its track where the relativistic-electron dropout and recovery from dropout occur are indicated. (See Table 1 for details.)

Table 1. Typical Chronology of a Recurring High-Speed-Stream Cycle and the Resulting Geomagnetic Activity, Behavior of the Earth's Plasma Sheet, Behavior of the Drainage Plumes, and Phase of the Relativistic-Electron Dropout

The Solar Wind at Earth	Stage of Geomagnetic Activity	Solar-Wind Density	Superdense Status	Plume Status	Relativistic-Electron-Dropout Status
Slow wind	Calm occurs ~70% of time	Density modest	Ordinary density Ordinary temperature	Plasmasphere growing	Relativistic-electron flux slow decay
CIR starts	Calm ends	Density modest	Ordinary density Ordinary temperature	Plasmasphere	Relativistic-electron flux slow decay
Compressed slow wind (westward flow)	Mild geomagnetic activity	Density rising	Ordinary density Ordinary temperature	Plasmasphere	Relativistic-electron flux slow decay
Sector reversal in compressed slow wind	Geomagnetic activity rises	Density high	Superdense starts Superhot starts	Plasmasphere	Relativistic-electron flux slow decay
Compressed slow wind with southward IMF	Storm onset	Density high	Superdense Superhot	Plume starts Plasma becomes lumpy	Onset of dropout
Stream interface (flow reversal)	Storm levels	Density declining	Superdense reaches dayside	Plume strong, lumpy	Dropout ongoing
Compressed fast wind (eastward flow)	Storm levels	Density modest	Superdense Superhot	Plume weakening, lumpy	Recovery of dropout commences
CIR ends	Storm levels	Density low Superhot continues	Superdense ceases	Plume weak and lumpy	Recovery progressing
Fast wind	Activity slowly declines	Density low	Ordinary density Superhot	Plume weak and lumpy	Recovery complete

onsets of relativistic-electron dropouts are associated with, to find out what the recoveries of relativistic-electron dropouts are associated with, and to explore the implications of these findings.

[8] This manuscript is organized as follows. In section 2 the data sets used for the study and the superposed epoch methods used are described. In section 3 the superposed epoch view of the solar wind and the magnetosphere during high-speed-stream-driven storms is presented. In section 4 superposed epoch analysis of the solar wind and magnetosphere triggered on the onsets of relativistic-electron dropouts and on the recoveries of relativistic-electron dropouts are presented. In section 5 the implications of the findings of the superposed epoch studies are discussed. In section 6 the findings are summarized and needed new research is outlined.

2. Data Sets and Event Selection for the Auperposed Epoch Analysis

[9] Relativistic-electron dropouts and recoveries are spotted and measured using the data set from the multispacecraft Synchronous Orbit Particle Analyzer (SOPA) [*Belian et al.*, 1992] in circular geosynchronous orbits (6.6 R_E) at the geographic equator. SOPA measures spin-averaged differential fluxes of electrons and of ions from 50 keV to 1.5 MeV every 10 seconds. The SOPA electron-flux measurements used here were provided by R. Friedel (private communication, 2007). For each year of data, the 1.1–1.5 MeV flux measurements on each of 7 spacecraft in operation were normalized so that all spacecraft had the same yearly averaged logarithm of the flux in the dawn sector. For some analysis, the SOPA fluxes on the individual spacecraft are used. Additionally, half-hour running averages of the measurements on each satellite were used to construct a multispacecraft logarithmic average (sum of log-fluxes divided by number satellites) of all the available fluxes at any time. The multispacecraft average flux was cleaned by removing times of known solar-energetic-particle events.

[10] The ion and electron plasma sheets and the plasmasphere and plasmaspheric drainage plumes in the dipolar magnetosphere are analyzed using the multispacecraft Magnetospheric Plasma Analyzer (MPA) data set [*Bame et al.*, 1993] in circular geosynchronous orbits (6.6 R_E) at the geographic equator. The MPA instruments measure three-dimensional ion and electron distribution functions every 86 seconds over the energy range 1 eV to 40 keV. Each distribution function is acquired in 10 seconds. MPA measurements from 7 spacecraft are used in the present analysis.

[11] The state of magnetospheric activity is measured with the use of the Kp and Dst indices. The Kp index is converted into a real number.

[12] The 1-minute OMNI database [*King and Papitashvili*, 2005] is used to obtain the properties of the solar wind plasma and the interplanetary magnetic field (IMF) at the Earth.

[13] The collection of high-speed-stream-driven storms used for the present study is the set of 124 recurring storms used for the superposed epoch studies of *Denton and Borovsky* [2008a, 2008b]. The storms are from the years 1993, 1994, 1995, 1996, 2003, 2004, 2005, and 2006. Realizing that high-speed-stream-driven storms are inefficient at producing Dst perturbations [*Borovsky and Denton*, 2006], these 124 high-speed-stream-driven storms were chosen according to magnetospheric convection, ignoring the Dst perturbations during the event selection. (This is in contrast to other superposed epoch studies [e.g., *Miyoshi and Kataoka*, 2005; *Denton et al.*, 2006; *Zhang et al.*, 2006; *Yermolaev et al.*, 2007; *Longden et al.*, 2008] which selected high-speed-stream-driven storms according to their Dst perturbations and focused the analysis on timing with respect to the Dst perturbations.) The 124 recurring storms were found by using the McPherron list of solar wind stream interfaces [R. McPherron, private communication, 2007; *McPherron and Weygand*, 2006] and then examining

temporal plots of the Kp index to identify storms following the stream interfaces. Only storms that are preceded by and/or followed by another storm 27 days earlier or later are accepted into the collection. Then, for each storm in the collection, the onset time of convection (storm onset) is determined from a drop in MBI (midnight boundary index). MBI is an index created from locations of the low-latitude edge of the diffuse auroral precipitation as determined by DMSP-satellite overflights, mathematically shifted to local midnight [*Gussenhoven et al.*, 1983]. MBI is a proxy for the position of the inner edge of the electron plasma sheet [*Elphic et al.*, 1999], which makes it an excellent indicator of magnetospheric convection, as is Kp [*Thomsen*, 2004], but MBI has higher time resolution than the 3-hour Kp index. The storm onset times were determined to about 30-minute accuracy.

[14] Subsets of events were collected based on properties of dropouts during the 124 storms. In particular a set of 33 events with strong onsets of the relativistic-electron dropout was selected, a set of 14 events that had strong relativistic-electron recoveries was selected, and a set of 10 events in which no dropouts nor recoveries occurred was selected.

[15] For the superposed epoch analysis of the data sets, three types of triggers (zero epochs) will be used: (1) triggering on storm onset as determined by increases in MBI (onsets of convection), (2) triggering on relativistic-electron-dropout onsets as seen in the multisatellite average of the 1.1–1.5 MeV electron flux, and (3) triggering on relativistic-electron recoveries as seen in the multisatellite average of the 1.1–1.5 MeV electron flux.

3. Superposed Epoch View of High-Speed-Stream-Driven Storms

[16] Figures 3 and 4 present an overview of high-speed-stream-driven storms. The various panels contain data superposed and averaged from 124 high-speed-stream-driven storms with the zero epoch (trigger) chosen to be the onset of storm levels of convection in the magnetosphere. The onset of storm levels of convection is taken to be when the Kp index reaches 4.3, but determined with the higher-resolution MBI. To do this a linear fit of MBI as a function of Kp is made for the 21 years 1983–2003, which yields MBI = 65.27 − 1.07Kp. According to the fit function, Kp increasing to 4.3 is equivalent to MBI decreasing to 60.68. The storm onset is then taken to be the first time at which MBI is lower than 60.68. In each panel of Figures 3 and 4 the zero epoch is indicated by a vertical dashed line.

[17] In Figures 3a to 3d, some solar wind parameters are plotted. Figure 3a shows the superposed average of the solar wind speed. As can be seen, prior to the storm the solar wind speed is low (~400 km/sec on average) and the storm onset occurs as the solar wind speed is ramping up. The

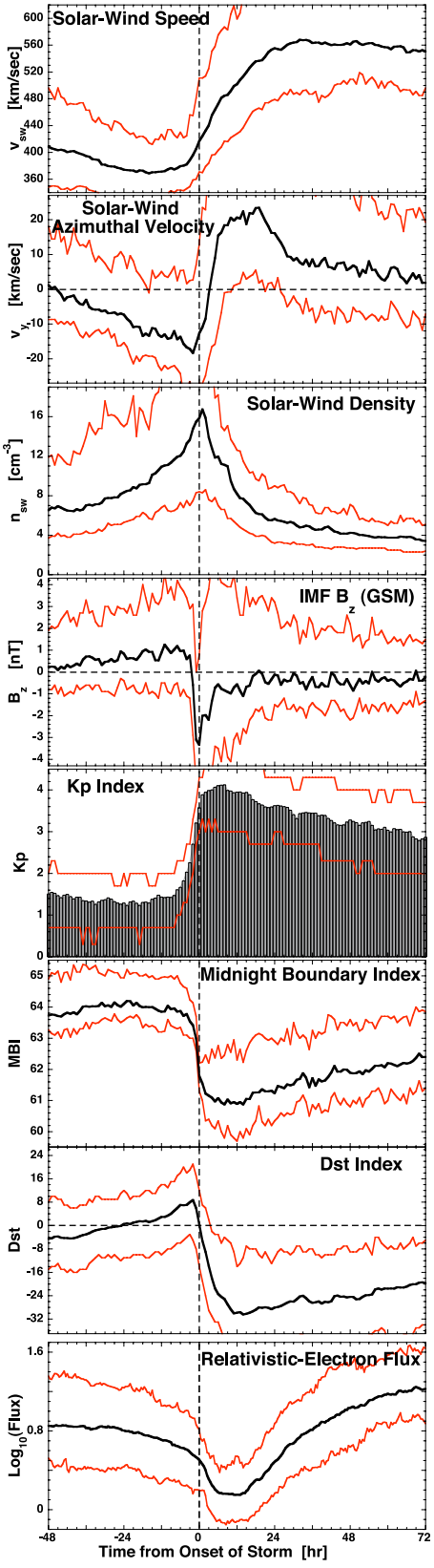

Figure 3. For 124 high-speed-stream-driven storms, superpositions of several measurements are plotted: in each figure, the black curve is the mean and the red curves are the upper and lower quartiles. From top to bottom, the eight panels contain the solar wind speed, the solar wind azimuthal (east-west or ecliptic) flow velocity, the solar wind number density, the z-component (GSM) of the solar wind magnetic field, the Kp index, the midnight boundary index, the Dst index, and the multisatellite average of the 1.1–1.5 MeV electron flux at geosynchronous orbit. The trigger for the data superposition (epoch = 0) is the onset of storm levels of convection in the magnetosphere.

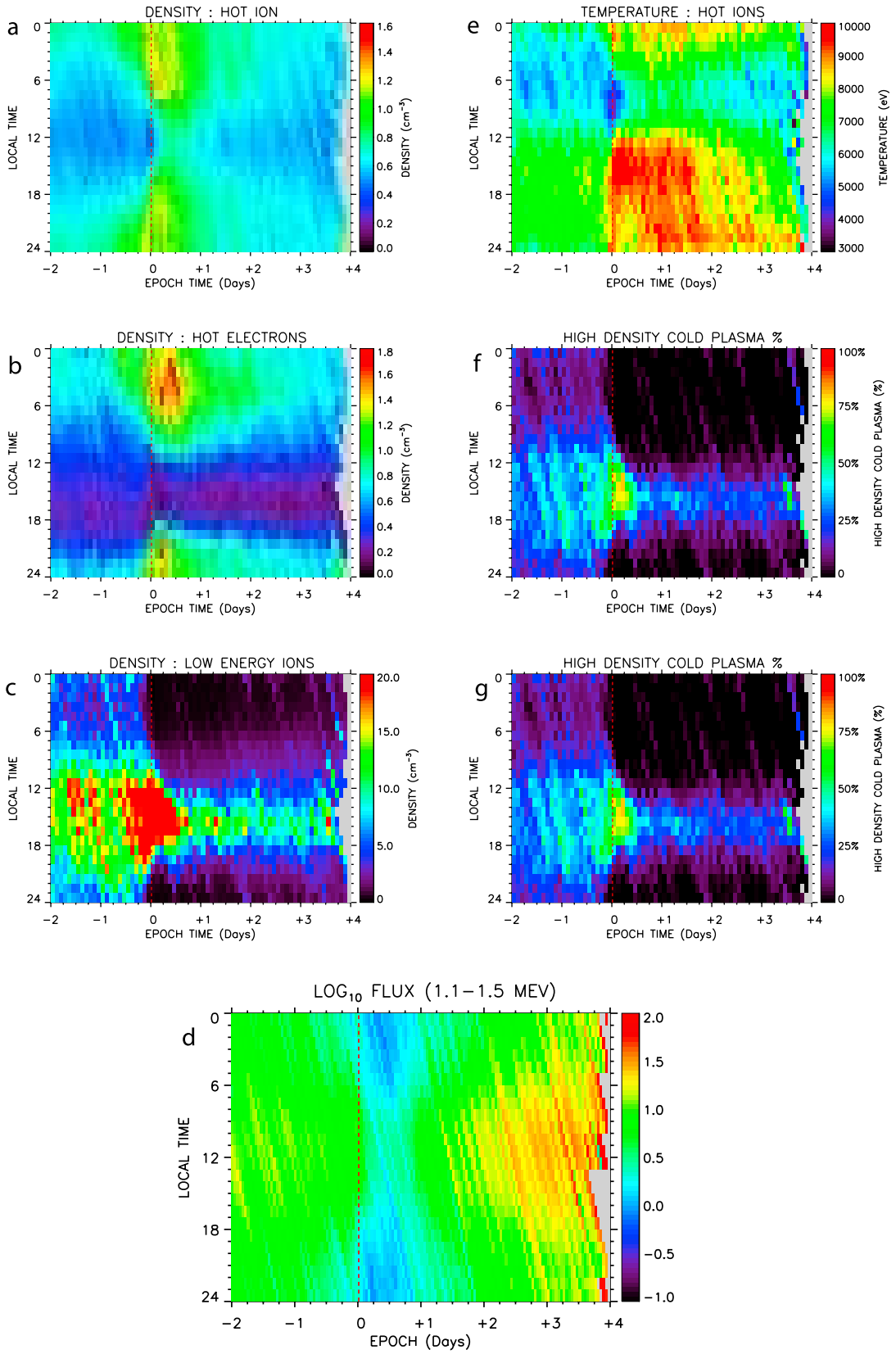

Figure 4. For 124 high-speed-stream-driven storms, superpositions of several measurements are plotted. (a, e) Density and temperature of the hot ions (0.1–45 keV) around geosynchronous orbit. (b, f) Density and temperature of the hot electrons (0.03–45 keV) around geosynchronous orbit. (c, g) Number density of the cold ions (1–100 eV) around geosynchronous orbit and the fraction of time that that density is measured to be greater than 10 cm^{-3}. (d) Flux of 1.1–1.5 MeV electrons around geosynchronous orbit.

high-speed-stream-driven storms last for several days and the solar wind speed is high (~550 km/sec on average) during the storms. Figure 3b contains a plot of the superposed average of the GSE y-component (ecliptic component) of the solar wind velocity. Note the characteristic westward-then-eastward deflection of the solar wind that is the signature of the corotating interaction region (CIR) between the slow wind and the fast wind [*Siscoe et al.*, 1969]. The point where the v_y flow reverses from westward to eastward through zero is the stream interface [e.g., *Burlaga*, 1974]. Note in this superposed average that the storm onset (dashed line) occurs about 3 hours prior to the passage of the stream interface (see also *Denton and Borovsky* [2008b]). In Figure 3c, the superposed average of the solar wind number density is plotted. The solar wind is compressed in the CIR by the dynamic-pressure difference of the fast wind overtaking the slow wind and so the density is increased [*Hundhausen*, 1973; *Richter and Luttrell*, 1986]. Prior to the passage of the stream interface the high density is compressed slow wind and any high density after the interface is compressed fast wind.

[18] In Figure 3d, the superposed average of the z-component (GSM coordinates) of the solar wind magnetic field B_z is plotted. Prior to the storm onset there is an interval of northward B_z that ends a few hours before storm onset and at storm onset there is a distinctly southward interval. The reversal from north to south (GSM) prior to the storm onset is the sector reversal of the IMF that typically occurs prior to the stream interface [*Gosling et al.*, 1978; *Neugebauer et al.*, 2004]. High-speed-stream-driven storms are owed to a Russell-McPherron effect of a Parker-spiral-orientation of the magnetic field seen in GSM coordinates: southward B_z after the sector reversal creates the storm [*Crooker and Cliver*, 1994; *McPherron and Weygand*, 2006] and northward B_z prior to the sector reversal creates a "calm before the storm" [*Borovsky and Steinberg*, 2006].

[19] In Figures 3e and 3f, two geomagnetic indices are plotted. In Figure 3e, the superposed average of the Kp index is plotted. As can be seen, Kp is elevated after the storm onset and Kp is low prior to the storm onset. Kp is a measure of the strength of convection in the magnetosphere [*Thomsen*, 2004], which is a measure of the strength of the solar wind driving of the magnetosphere. In Figure 3f, the superposed average of the Dst index is plotted. Prior to the high-speed-stream-driven storm there is an interval in which Dst is positive indicating that the weakly driven magnetosphere is compressed [*Borovsky et al.*, 1998a]. At storm onset Dst reverses to negative indicating the magnetospheric convection is increasing the pressure of magnetospheric plasmas to produce a diamagnetic effect [*Sckopke*, 1966]. Note two things about the Dst signature of the storms. First, note that the negative Dst signature is modest; unlike CME-driven storms, high-speed-stream-driven storms typically do not produce strong Dst perturbations [*Yermolaev and Yermolaev*, 2002; *Denton et al.*, 2006; *Borovsky and Denton*, 2006]. Second, note that the negative-Dst perturbation is sustained for days during the storm. Unlike a true recovery of Dst which is caused by convection shutting down and the ring-current plasma decaying [e.g., *Liemohn et al.*, 1999; *Kozyra and Liemohn*, 2003], Dst in high-speed-stream-driven storms is, for days, maintained in a sustained equilibrium between driving and loss [cf. *Turner et al.*, 2006].

[20] In the bottom panel of Figure 3h, the superposed average from the 124 storms of the multisatellite average of the logarithm of the 1.1–1.5 MeV electron flux at geosynchronous orbit is plotted. Note that the flux drops just after storm onset, goes through a recovery at about 1 day after storm onset, and then grows in magnitude slowly over a several-day interval during the storm. In individual storms the dropout onset and the recovery are much more rapid than they are in this superposed average; in this plot they are smoothed owing to variations in the timing of the dropout onset and the dropout recovery relative to the storm onset, which is the trigger for the superposition. Note in Figure 3h the slow decay of the relativistic-electron flux prior to the onset of the storm: this decay is owed to pitch-angle scattering by plasma waves in the quiet magnetosphere prior to the storm [cf. *Meredith et al.*, 2006]. On days when a built-up outer plasmasphere is present this decay is more rapid [*Borovsky and Steinberg*, 2006].

[21] In the seven panels of Figure 4 the plasmas and the relativistic-electron flux around geosynchronous orbit are examined for the 124 storms as functions of local time and storm epoch. The zero epoch is the onset of storm convection. In Figure 4a, the hot-ion (0.1–45 keV) density measured around geosynchronous orbit by MPA is displayed. Prior to the storm the densities are at typical levels (densities of 1 cm^{-3} or less on the nightside and densities of 0.5 cm^{-3} or less on the dayside [e.g., *Thomsen et al.*, 1996; *Maurice et al.*, 1998; *Korth et al.*, 1999]) and about a day or so after storm onset the densities are again at typical levels. However, during the first day after storm onset the superposed average density is anomalously high. This is the so-called "superdense plasma sheet" (where "superdense" was defined to mean "of anomalously high density" [*Borovsky et al.*, 1997; *Denton and Borovsky*, 2008b]). The superdense plasma sheet originates from extra-high-density solar wind plasma (see Figure 3c) which enters the magnetosphere with a several-hour time lag [*Borovsky et al.*, 1998b], during high-speed-stream-driven storms in particular [*Denton and Borovsky*, 2008b]. In Figure 4e, the superposed average temperature of the ions measured around geosynchronous orbit by MPA is displayed. Prior to storm onset the ion temperatures are typical: about 7 keV [*Thomsen et al.*, 1996; *Korth et al.*, 1999; *Denton et al.*, 2005, 2006]. However, the ion temperature is anomalously hot beginning at about storm onset and the temperature remains anomalously hot for the several-day duration of the storm. This is the so-called "extra-hot phase" of the plasma sheet [*Denton and Borovsky*, 2008b] (where "extra-hot" was defined to mean "anomalously hot"). The extra-hot plasma sheet is a result of the high speed of the solar wind [*Borovsky et al.*, 1998b; *Denton and Borovsky*, 2008b]. Note that the superdense plasma sheet seen in Figure 4a is hot (as in the study by *Borovsky et al.* [1997]) and should not be confused with the "cool dense plasma sheet" of the outer magnetosphere [*Fujimoto et al.*, 2000, 2002, 2005; *Nishino et al.*, 2002; *Phan et al.*, 2000] that sometimes briefly appears at geosynchronous orbit during the early phases of storms [e.g., *Thomsen et al.*, 2003; *Borovsky and Steinberg*, 2006; *Lavraud et al.*, 2005, 2006].

[22] High-density magnetospheric plasma is important for the production of a robust ring current and a negative Dst perturbation [e.g., *Borovsky et al.*, 1997; *Kozyra et al.*, 1998; *Thomsen et al.*, 1998a; *Ebihara et al.*, 2005]. Note that the fact the superdense plasma sheet is so hot probably contributes to the fact that high-speed-stream-driven storms do not produce large Dst perturbations [*Borovsky and Denton*, 2006]: magnetospheric convection does not lead to as much plasma compression when the plasma is hot [e.g., *Ebihara and Ejiri*, 2000; *Kozyra and Liemohn*, 2003; *Lavraud et al.*, 2006; *Lavraud and Jordanova*, 2007].

[23] The hot-electron (0.03–45 keV) behavior around geosynchronous orbit as measured by MPA is displayed in Figures 4b and 4f. Figures 4b and 4f show a behavior that is very similar to that of the hot ions in the top row. The hot-electron density is normal before the storm onset, is superdense for about a day after storm onset, and is normal after about a day after the onset, and the temperature is normal before the storm onset and is in a extra-hot phase beginning at the onset of the storm and lasting for days as the storm lasts. Note that this extra-hot electron plasma sheet gives rise to high levels of spacecraft charging during high-speed-stream-driven storms [*Borovsky et al.*, 1998a; *Denton et al.*, 2006; *Borovsky and Denton*, 2006]. Note also in Figure 4b that the density of hot electrons on the dayside is much less then the density on the nightside. This is because the plasma-sheet electrons suffer substantial loss to the atmospheric loss cone as they are transported from the nightside around to the dayside [*Thomsen et al.*, 1998b; *Longden et al.*, 2008].

[24] The cold-plasma (1–100 eV) (plasmasphere and plasmaspheric-drainage-plume) behavior around geosynchronous orbit measured by MPA is displayed in Figures 4c and 4g. In Figure 4c, the superposed average of the cold-ion number density is plotted and in the right column the fraction of time that the cold-ion density is observed to be above 10 cm^{-3} is plotted. As can be seen in Figure 4g, prior to storm onset there is a probability of seeing plasmaspheric plasma at all local times; during the storm the plasmaspheric material is only found in the post-noon sector in the form of a drainage plume [e.g., *Chappell*, 1974; *Chen and Grebowsky*, 1974; *Spiro et al.*, 1981; *Elphic et al.*, 1996]. Prior to the storm the plasmasphere proper is seen at geosynchronous orbit: if geomagnetic activity is very low then the plasmasphere can be seen at all local times [cf. *Sojka and Wrenn*, 1985; *Su et al.*, 2001] and if geomagnetic activity is modest then the plasmasphere is only encountered at the "dusk bulge" [cf. *Chappell et al.*, 1970; *Higel and Lei*, 1984; *Carpenter et al.*, 1993]. During a high-speed-stream-driven storm, there is essentially always a plasmaspheric drainage plume crossing geosynchronous orbit in the post-noon sector [*Borovsky and Denton*, 2008] early in the storm the plume is dense and broad (in local time) and later in the storm it is less dense and narrower. Hence, in the superposed epoch average (third row) the probability of seeing plume material in the post-noon sector is high and the average density there is high and later in the storm the probability of being in plume plasma is lower and the average density is lower. Note that whenever drainage-plume plasma is encountered, it is very lumpy with strong gradients in the plasma density [*Borovsky and Denton*, 2008].

[25] In Figure 4d, the logarithm of the 1.1–1.5 MeV electron flux around geosynchronous orbit measured by SOPA is displayed. Prior to the storm onset, the level of flux is steady or slowly declining [cf. *Meredith et al.*, 2006; *Borovsky and Steinberg*, 2006]. At storm onset the flux drops rapidly (see also Figure 3h, which is the multisatellite average of the logarithm of the flux). After about a day the flux recovers. Note the flux growing in intensity in the days following the dropout recovery.

[26] From this examination of Figures 3 and 4, it is found that the relativistic-electron dropouts are temporally associated with (1) magnetospheric convection (as measured by Kp) reaching high levels, (2) the appearance of the superdense extra-hot ion plasma sheet (which is in turn associated with the high-density solar wind with a few-hour time lag [*Denton and Borovsky*, 2008b]), (3) the appearance of the superdense extra-hot electron plasma sheet (which is also associated with the high-density solar wind with a few-hour time lag [*Denton and Borovsky*, 2008b]), (4) the onset of a plasmaspheric drainage plume, and (5) the storm time increase in the magnitude of Dst.

[27] Using three subsets of events and triggering the superposed epoch averages on the dropout onsets and on the dropout recoveries, these temporal associations will be explored in section 4. Also, by triggering on the onsets and recoveries, the relativistic-electron dropouts can be better placed in the timeline of the geomagnetic storm and of the changing solar wind plasma and magnetic field of the CIR.

4. Superposed Epoch Study of Special Events

[28] From the 124 high-speed-stream-driven storms utilized in section 3, three subsets of events are selected for closer study in the following three subsections. The first is a collection of 33 storms that have very rapid onsets of the relativistic-electron dropouts. The second is a collection of 14 storms that have very rapid recoveries of the relativistic-electron flux. The third is a collection of 10 storms that have neither dropout nor recovery, i.e. the relativistic-electron fluxes were relatively unaffected during the storms. With the first collection in section 4.1, we will trigger the superposed averages on the dropout onsets to see what the dropouts are associated with. The "onset of dropout" will be taken to be the steepest part of the drop in the logarithm of the 1.1–1.5 MeV electron flux. With the second collection in section 4.2 we will trigger the superposed averages on the recoveries to see what the recoveries are associated with. The "onset of recovery" will be taken to be the steepest part of the rise in the logarithm of the 1.1–1.5 MeV electron flux. The findings from these two examinations will be contrasted in section 4.3 with the third set of events in which no dropouts nor recoveries happen. For this third set of events we cannot trigger on the dropout onset or recovery (since there are none) so the superposed averages will be triggered on the onset of storm convection, as were the 124 storms of section 3.

4.1. Triggering on Dropout Onsets

[29] The superposed average of the data when using the 33 events with sharp onsets of dropouts and triggering on the onset are displayed in top columns of Figures 5 and 6 and in left-hand columns of Figures 7, 8, 9, and 10. The

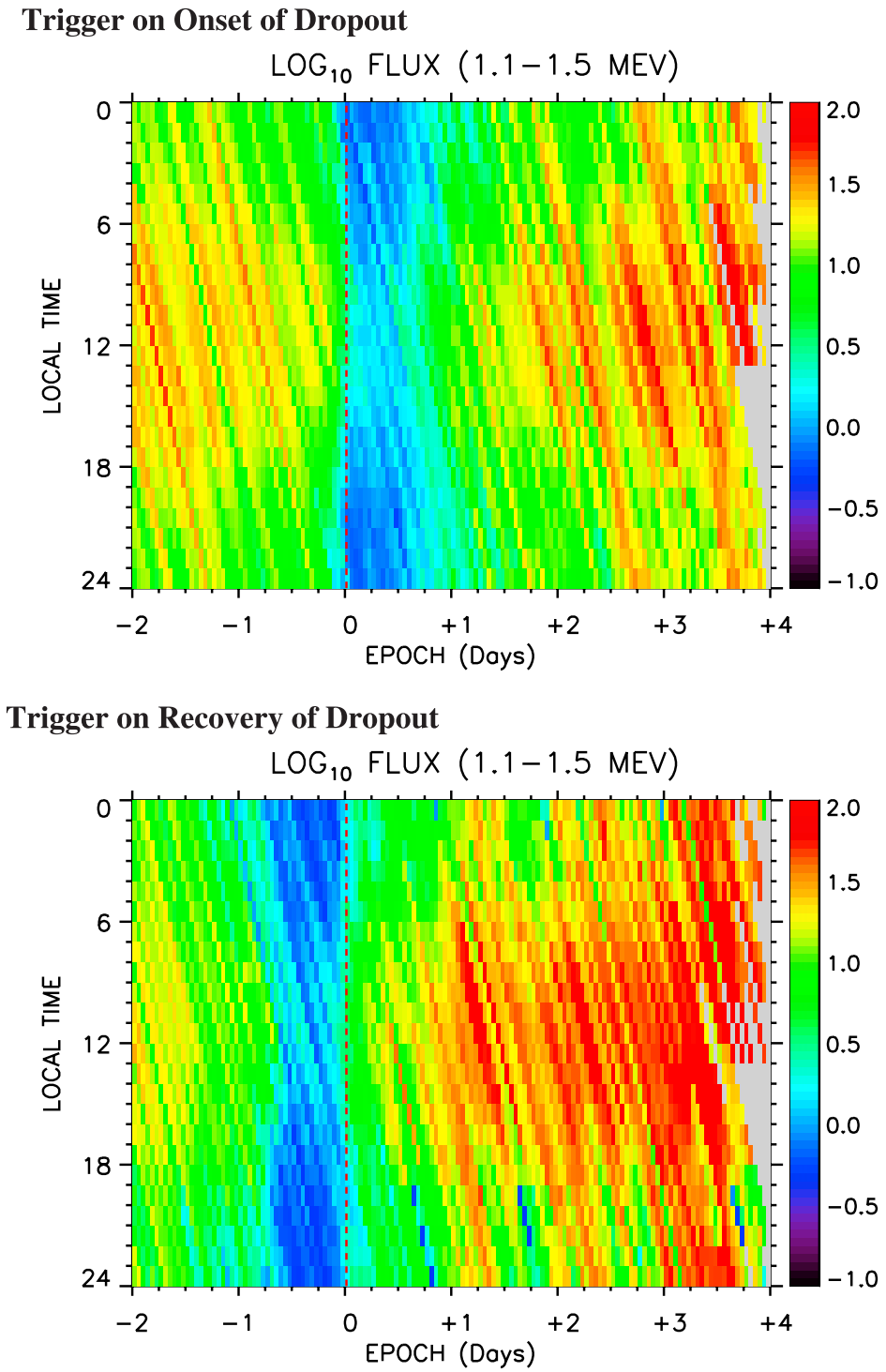

Figure 5. (top) Logarithm of the flux of 1.1–1.5 MeV electrons around geosynchronous orbit is plotted for a set of 33 events with clear onsets to relativistic-electron dropouts, with the triggering of the superposition being the onset of dropout. (bottom) Logarithm of the flux of 1.1–1.5 MeV electrons around geosynchronous orbit is plotted for a set of 14 events with clear recoveries to relativistic-electron dropouts, with the triggering of the superposition being the recovery from dropout.

zero epoch (= onset of dropout = steepest part of the drop) is denoted in each panel of those figures by a vertical dashed line.

[30] The superposed average of the logarithm of the 1.1–1.5 MeV electron flux measured by SOPA onboard the multiple satellites around geosynchronous orbit is shown in Figure 5 (top), with the zero epoch being the steepest part of the drop in the multisatellite average of the logarithm of the 1.1–1.5 MeV electron flux. As can be seen in Figure 5, the

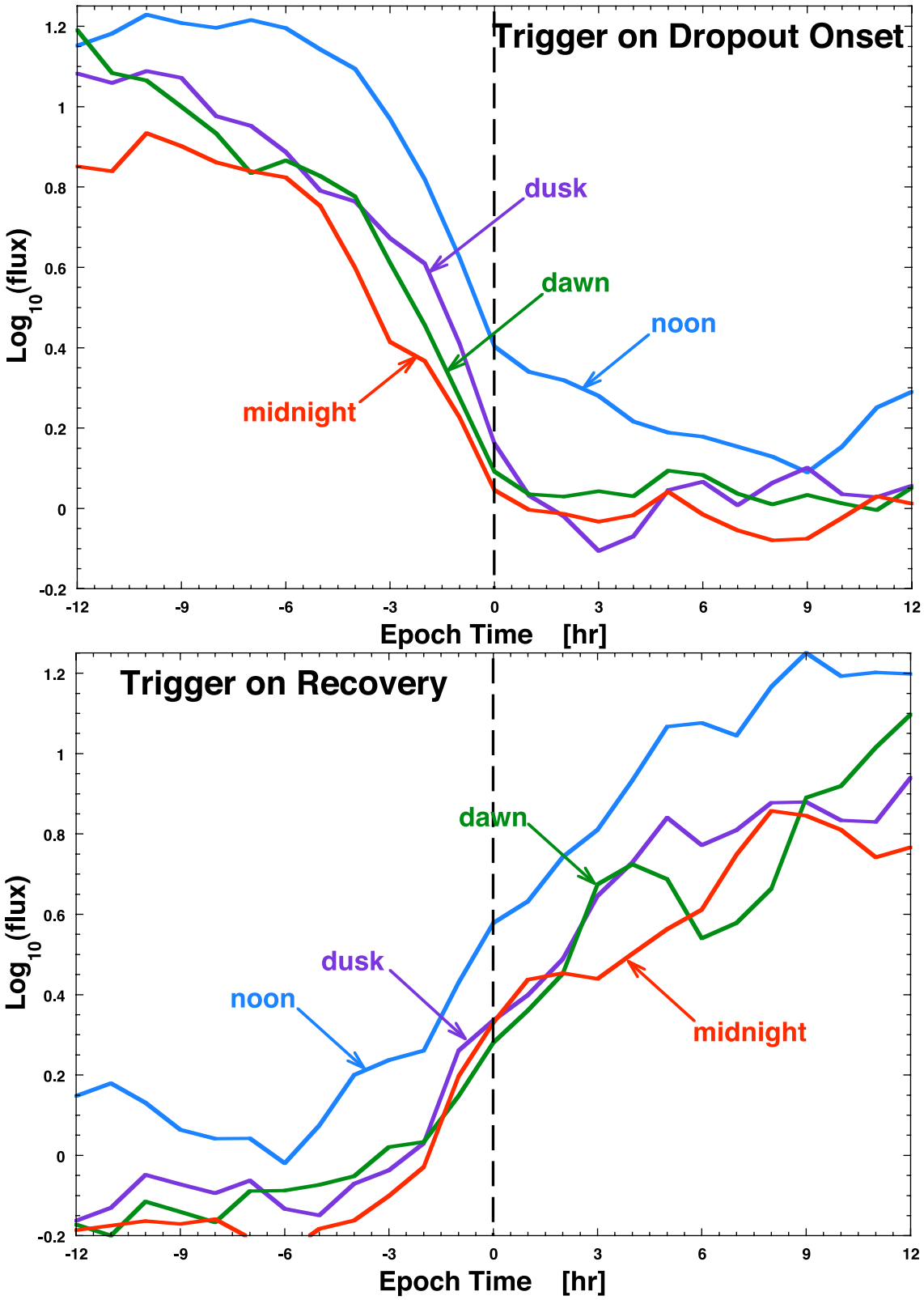

Figure 6. (top) Logarithm of the flux of 1.1–1.5 MeV electrons at geosynchronous orbit is plotted for a set of 33 events with clear onsets to relativistic-electron dropouts, with the triggering of the superposition being the onset of dropout. (bottom) Logarithm of the flux of 1.1–1.5 MeV electrons at geosynchronous orbit is plotted for a set of 14 events with clear recoveries to relativistic-electron dropouts, with the triggering of the superposition being the recovery from dropout. In both figures, the four color curves each represent a 5-hour-wide average in local time centered about midnight (0 LT), dawn (6 LT), noon (12 LT), and dusk (18 LT).

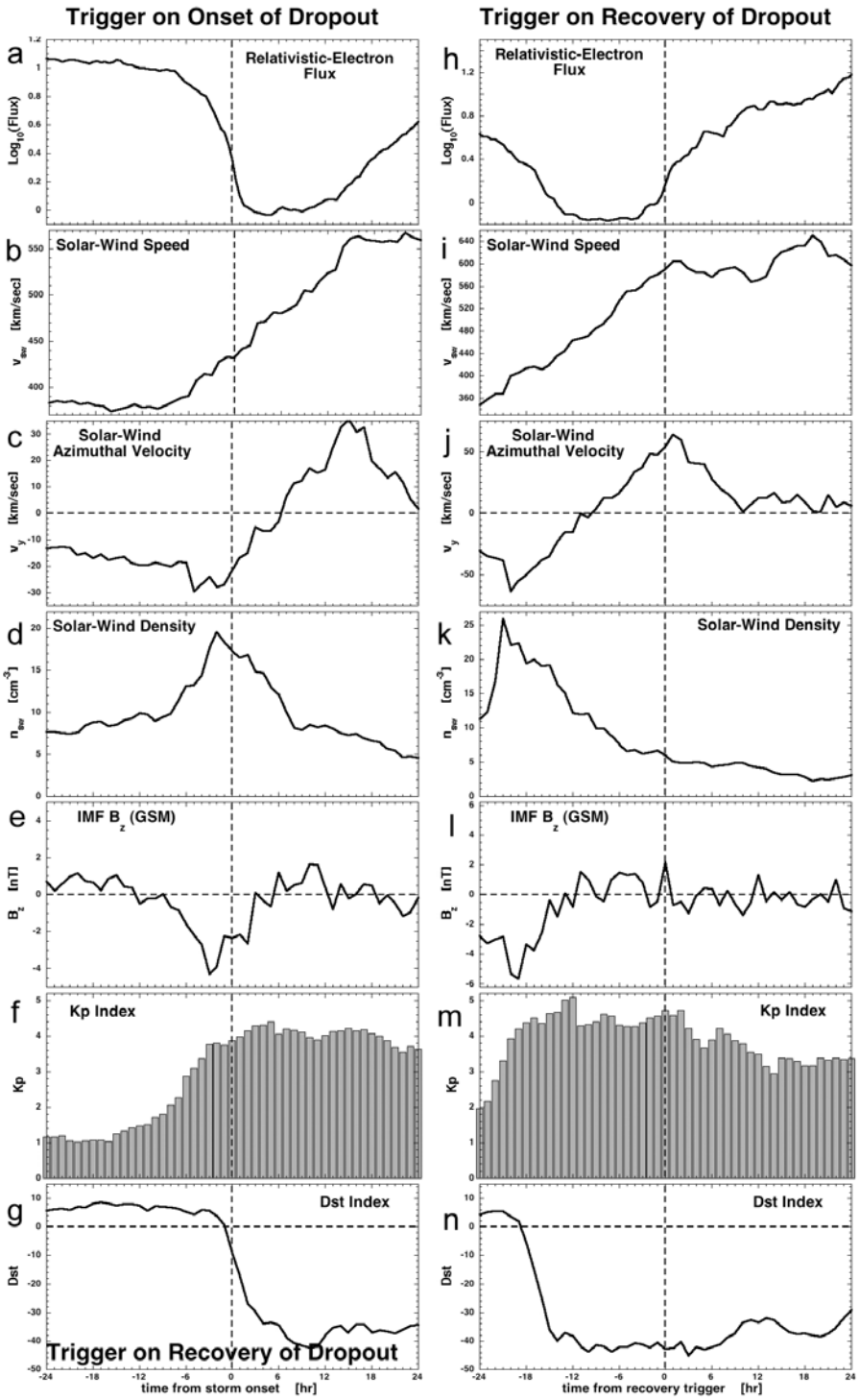

Figure 7. (left) Several parameters are plotted for 33 events with clear onsets with the triggering of the superposition being the onset of dropout. (right) Several parameters are plotted for 14 events with clear recoveries with the triggering of the superposition being the recovery of dropout. (a, h) Logarithm of the multisatellite average of the 1.1–1.5 MeV electron flux. (b, i) Solar wind speed. (c, j) East-west flow of the solar wind. (d, k) Number density of the solar wind. (e, l) z-Component (GSM) of the solar wind magnetic field. (f, m) Kp index. (g, n) Dst index.

dropout occurs at all local times. Owing to the systematic diurnal trend in the fluxes, it is difficult to see if there is a local-time dependence of the timing of the onset of dropout in Figure 5. In Figure 6 (top), the logarithm of the fluxes is averaged over 5 hours of local time centered at midnight (0 LT, red), dawn (6 LT, green), noon (12 LT, blue), and dusk (18 LT, purple) and plotted as functions of time from trigger. The curves from the four local-time sectors were fit

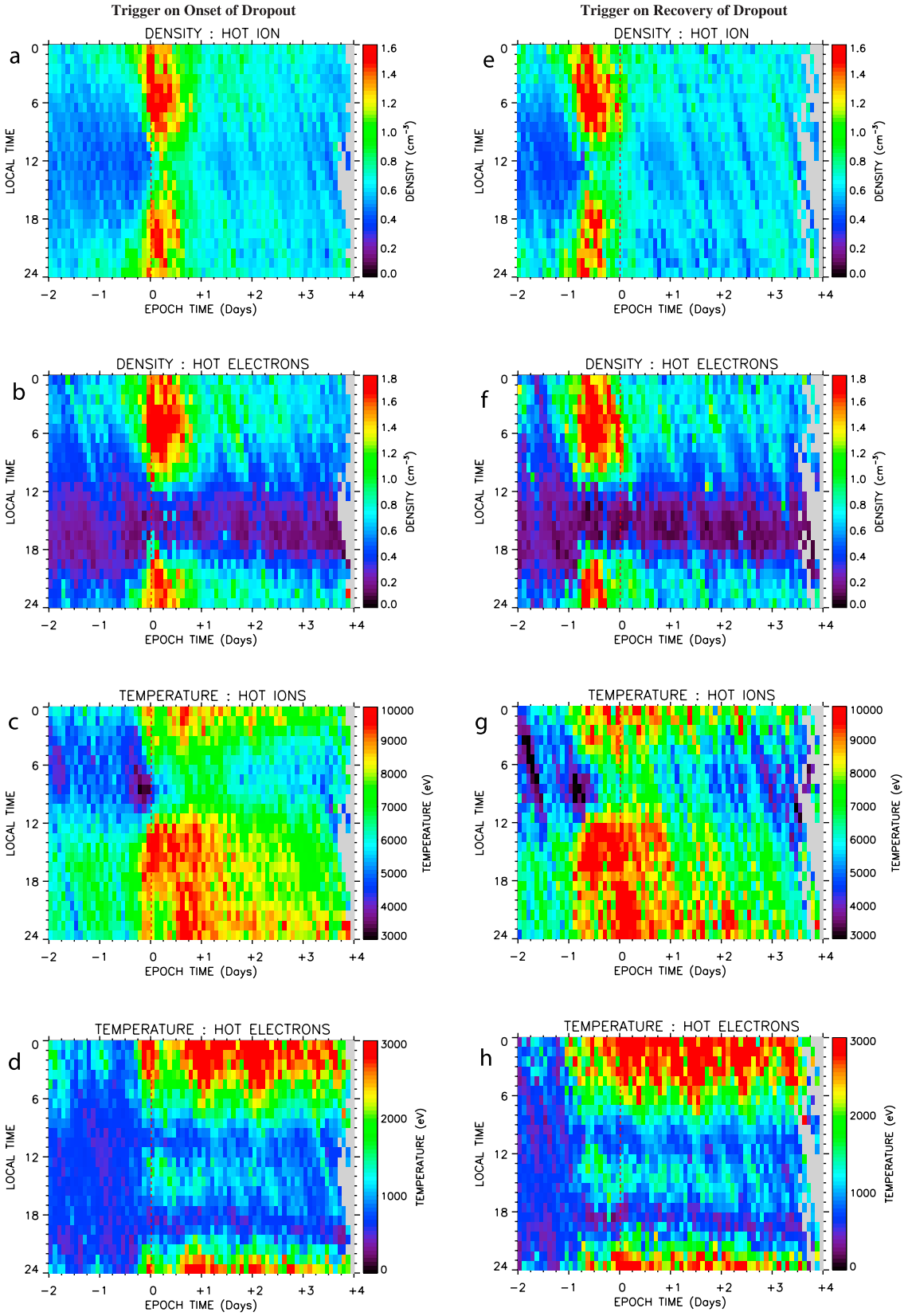

Figure 8. (left) Several parameters around geosynchronous orbit are plotted for 33 events with clear onsets with the triggering being the onset of dropout. (right) Several parameters around geosynchronous orbit are plotted for 14 events with clear recoveries with the triggering of the being the recovery from dropout. (a, e) Density of hot ions (0.1–45 keV) is plotted. (b, f) Density of hot electrons (0.03–45 keV) is plotted. (c, g) Temperature of hot ions is plotted. (d, h) Temperature of hot electrons is plotted.

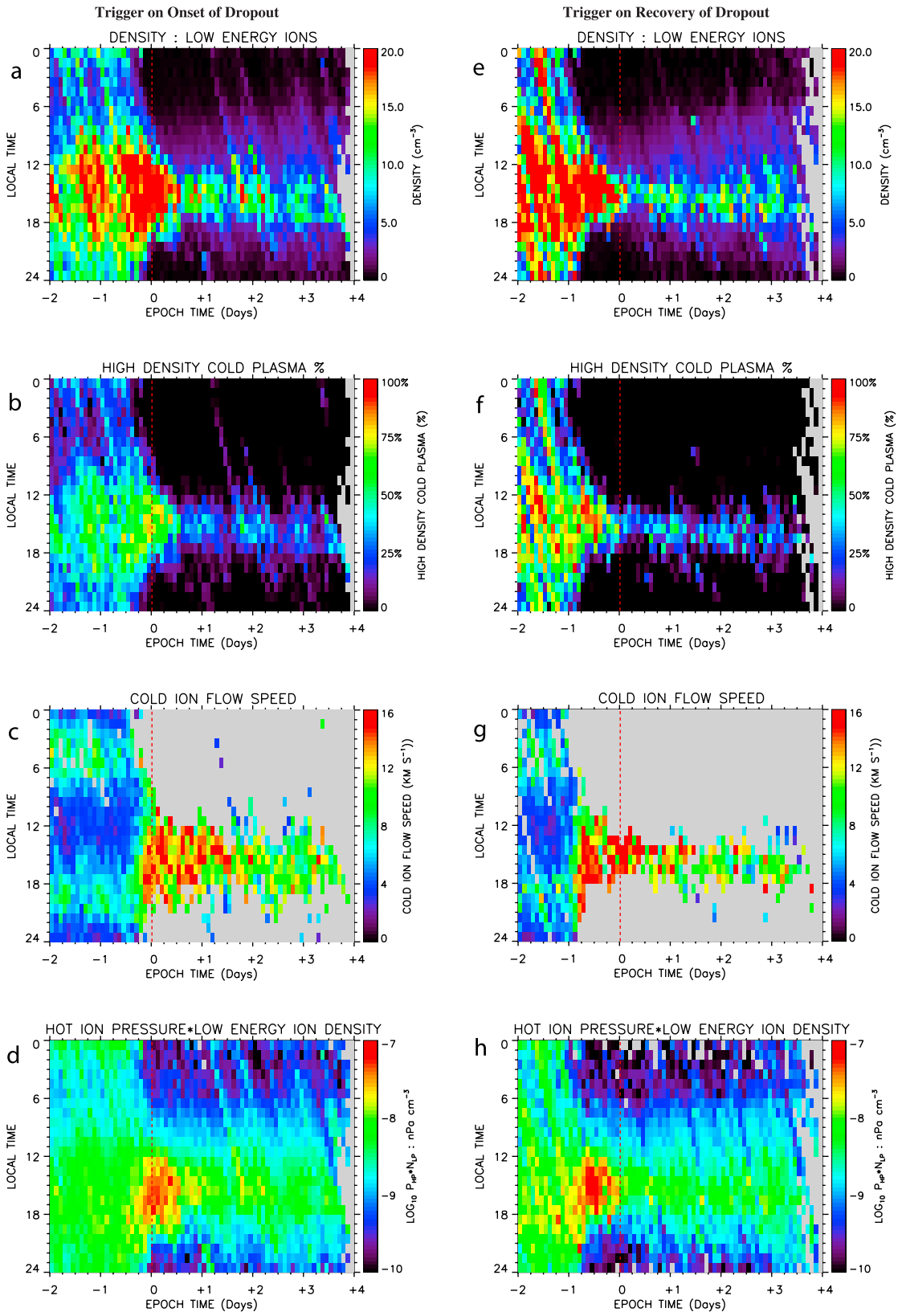

Figure 9. Several parameters around geosynchronous orbit are plotted (left) for 33 events with clear onsets with the triggering being the onset of dropout. and (right) for 14 events with clear recoveries with the triggering of the being the recovery of dropout. (a, e) Density of cold ions (1–100 eV) is plotted. (b, f) Percent of time that the cold-ion density is above 10 cm^{-3} is plotted. (c, g) Flow velocity of the cold ions (only when their density is greater then 10 cm^{-3}) is plotted. (d, h) Logarithm of the product of the hot-ion (0.1–45 keV) pressure and the cold-ion density is plotted.

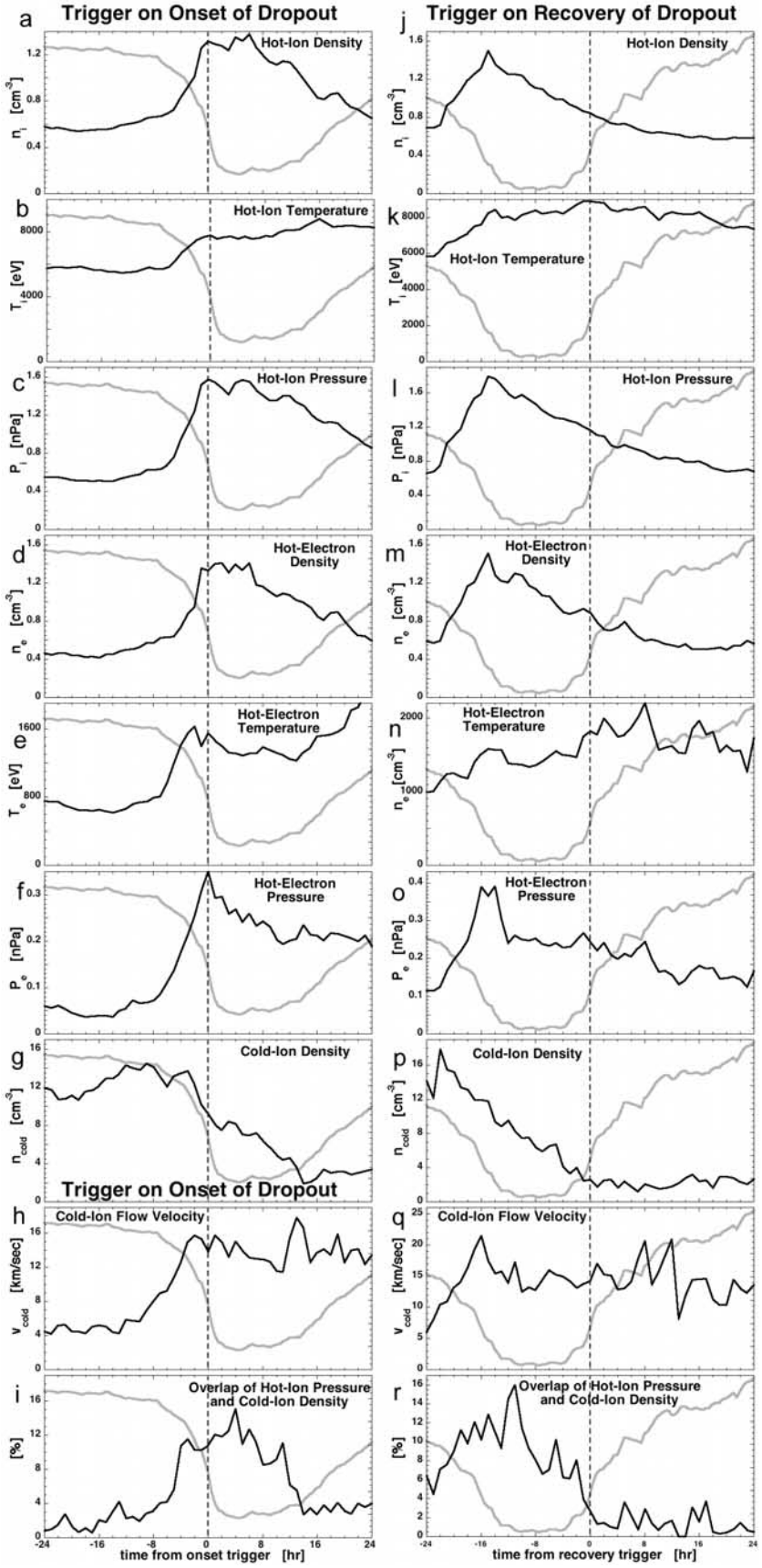
a
Trigger on Onset of Dropout
Hot-Ion Density
n_i [cm^{-3}]
b
Hot-Ion Temperature
T_i [eV]
c
Hot-Ion Pressure
P_i [nPa]
d
Hot-Electron Density
n_e [cm^{-3}]
e
Hot-Electron Temperature
T_e [eV]
f
Hot-Electron Pressure
P_e [nPa]
g
Cold-Ion Density
n_{cold} [cm^{-3}]
Trigger on Onset of Dropout
h
Cold-Ion Flow Velocity
v_{cold} [km/sec]
i
Overlap of Hot-Ion Pressure and Cold-Ion Density
[%]
-24 -16 -8 0 8 16 24
time from onset trigger [hr]
j
Trigger on Recovery of Dropout
Hot-Ion Density
n_i [cm^{-3}]
k
Hot-Ion Temperature
T_i [eV]
l
Hot-Ion Pressure
P_i [nPa]
m
Hot-Electron Density
n_e [cm^{-3}]
n
Hot-Electron Temperature
n_e [cm^{-3}]
o
Hot-Electron Pressure
P_e [nPa]
p
Cold-Ion Density
n_{cold} [cm^{-3}]
q
Cold-Ion Flow Velocity
v_{cold} [km/sec]
r
Overlap of Hot-Ion Pressure and Cold-Ion Density
[%]
-24 -16 -8 0 8 16 24
time from recovery trigger [hr]

Figure 10

with hyperbolic-tangents to determine the widths of the drops in flux and the relative timing of the onsets. It is found that the widths of the drops in the four regions vary from 5.7–7.7 hr. The temporal centers of the drops are within 1.77 hours of each other, with the drop at dawn occurring first, then midnight, then dusk, and then noon. Note, the relative timings determined may not be statistically significant.

[31] In Figure 7a, the superposed average of the logarithm of the multisatellite averaged 1.1–1.5 MeV electron flux at geosynchronous orbit is plotted. The zero epoch (trigger) for the superposition of data is the steepest part of the drop in the logarithm of the flux. As can be seen, when superposing on the onsets of the dropouts, the abruptness of the onsets is evident. In Figure 7a, the dropout recovery appears gradual owing to the mixed timings of the individual recoveries. When the recoveries are used as the trigger (see Figure 7h), then the rapidity of the recoveries will be seen.

[32] In Figures 7b to 7e, the superposed averages of some solar wind parameters are plotted triggered on relativistic-electron-dropout onsets. Figure 7b shows the solar wind speed. As can be seen, the onset of the dropout (vertical dashed line) occurs while the solar wind speed is increasing. Figure 7c shows that the onset of dropout occurs in the CIR during the westward flow deflection of the solar wind. In the superposed average, the onset of dropout (steepest part of the drop) occurs about 6 hours prior to the passage of the stream interface (reversal of v_y through zero). Analyzing the 33 individual events that go into the superposed average, the onset of dropout (steepest part of the drop) occurs 4.6 ± 5.7 hours prior to the passage of the stream interface (where A ± B is the mean value ± one standard deviation). This means that the onset occurs during the passage of the compressed slow wind in the CIR. This is noted in Table 1 and is noted in the CIR sketch of Figure 2. Figure 7d shows the superposed average of the solar wind density. Note the pulse of high-density solar wind. Comparing this Figure 7d with the Figure 7c, it is seen that most of the high-density solar wind occurs prior to the passage of the stream interface (v_y reversal through zero), meaning that most of the high-density solar wind is compressed slow wind. This is noted in Table 1. As can be seen in Figure 7d, the dropout onset occurs while the solar wind density is high. Note that the onset of dropout occurs about 6 to 8 hours after the solar wind density begins to rise. Figure 7e shows that the relativistic-electron drop onset occurs during the passage of the pulse of strong $-B_z$ in the solar wind. In the superposed averages of Figure 7e, this dropout onset (steepest part of the drop) occurs about 9 hours after the passage of the sector reversal (where B_z crosses through zero to turn negative). Analyzing the individual events that go into the superposed average, the onset of dropout occurs 7.3 ± 8.4 hours after to the passage of the sector reversal. This is noted into Table 1 and is noted in the CIR sketch of Figure 2.

[33] In Figures 7f and 7g, the superposed average of the geomagnetic indices Kp and Dst are displayed, with the data superposition triggered on the relativistic-electron-dropout onset. As can be seen in Figure 7f, the onset of dropout occurs just about as the Kp index is reaching its maximum value; i.e. the dropout onset (steepest part of the drop) occurs when the magnetospheric convection is reaching its maximum value. This is noted in Table 1. As can be seen in Figure 7g, the dropout onset occurs as the Dst index is making its rapid descent to negative values.

[34] In the left-hand column of Figure 8, the density and temperature of the hot ions (ion plasma sheet) and hot electrons (electron plasma sheet and electron trough) around geosynchronous orbit as measured by MPA are shown, with the zero epoch (trigger) of the data superposition being the onset of the relativistic-electron dropout. As can be seen in Figures 8a and 8b, the onset of dropout is approximately simultaneous with the appearance of the superdense ion plasma sheet at geosynchronous orbit and the appearance of the superdense electron plasma sheet at geosynchronous orbit. In addition, as can be seen in Figures 8c and 8d, the relativistic-electron-dropout onset is approximately simultaneous with the onset of the extra-hot phase of the ion plasma sheet at geosynchronous orbit and the extra-hot phase of the electron plasma sheet at geosynchronous orbit. These facts are noted in Table 1. Depending on local time, the extra-hot phase usually commences about 3 hours after the superdense phase at geosynchronous orbit for high-speed-stream-driven storms [*Denton and Borovsky*, 2008b]. The timing of the onsets of relativistic-electron dropouts relative to the superdense and extra-hot plasma-sheet onsets will be explored in Figure 10 later in this subsection.

[35] In Figure 9 (left), some of the properties of the cold-plasma measured around geosynchronous orbit by MPA are shown, with the zero epoch (trigger) of the data superposition being the onset of the relativistic-electron dropout. Figures 9a and 9e show the superposed average cold-plasma density. At the time of onset of the dropout, the dusk bulge of the plasmasphere is undergoing a narrowing in local-time extent into the plasmaspheric drainage plume in the post-noon sector. This same phenomena is seen again in Figure 9b, where the fraction of time that the cold-plasma density is observed to be above 10 cm^{-3} is shown: the onset of the relativistic-electron-dropout occurs as the dusk bulge is transitioning into the drainage plume. This is noted in Table 1. In Figure 9c, the superposed average of the flow speed of the cold-plasma measured at geosynchronous orbit is shown. At about the time of onset of the dropout, the plasmaspheric material begins to flow (owing to magneto-

Figure 10. Several parameters at geosynchronous orbit are plotted (left) for 33 events with clear onsets of dropouts (triggered on the onset) and (right) for 14 events with clear recoveries (triggered on the recovery). The parameters are all averaged over the full orbit, except the cold-ion flow velocities, which are averaged only over the 14–18 LT region. (a, j) Hot-ion (0.1–45 keV) density at geosynchronous orbit. (b, k) Hot-ion temperature at geosynchronous orbit. (c, l) Hot-ion pressure at geosynchronous orbit. (d, m) Hot-electron (0.03–45 keV) density at geosynchronous orbit. (e, n) Hot-electron temperature. (f, o) Hot-electron pressure. (g, p) Cold-ion (1–100 eV) density. (h, q) Cold-ion flow speed (only used when the density is greater than 10 cm^{-3}). (i, r) Fraction of time when the cold-ion density is greater than 10 cm^{-3} and the hot-ion pressure is greater then 1 nPa.

spheric convection). Note that when the plasmaspheric material flows, it becomes lumpy [*Borovsky and Denton*, 2008]. In Figures 9d and 9h, the superposed average of the product of the hot-ion pressure (in units of nPa) and the cold-ion density (in units of cm^{-3}) is plotted. This plot shows the times and regions where there is strong potential for the growth of electromagnetic ion-cyclotron (EMIC) waves: sufficient free energy in the hot ions and sufficient cold plasma [*Cornwall et al.*, 1970; *Fraser and Nguyen*, 2001]. Note that the color scale is logarithmic. As can be seen, this product increases noticeably at the time of onset of the relativistic-electron dropout.

[36] In the left-hand column of Figure 10 we will look for indications of what causes the relativistic-electron dropouts. Most quantities plotted in Figure 10 are ''orbit averaged'', that is they are averaged over all local times. To guide the eye, in each panel of the left-hand column the multisatellite average of the logarithm of the 1.1–1.5 MeV electron flux triggered on the onset of dropout is drawn in gray, and the trigger is drawn as the vertical dashed line. In Figures 10a-10c and 10j-10l, the orbit-averaged density, temperature, and pressure of the ion plasma sheet is plotted. As can be seen, the commencement of the superdense and extra-hot ion plasma sheet is simultaneous with the onset of relativistic-electron dropout. In Figures 10d-10f and 10m-10o, the orbit-averaged density, temperature, and pressure of the hot electrons is plotted. Likewise, the onset of the relativistic-electron dropout is simultaneous with the commencement of the superdense and extra-hot electron plasma sheet. In Figures 10g-10h and 10p-10q, the orbit-averaged cold-ion density and the cold-ion flow velocity averaged over the 14–18 LT regime are plotted. The onset of relativistic-electron dropout is simultaneous with the formation of plasmaspheric drainage plumes, signified by a dropping of the orbit-averaged cold-ion density and a commencement of the cold-ion flow velocity. Finally, Figures 10i and 10r, the fraction of time over the geosynchronous orbit that both the cold-ion density is greater then 10 cm^{-3} AND the hot-ion pressure is greater then 1 nPa is plotted. As can be seen, simultaneous with the onset of the relativistic-electron dropout the fraction of time high-pressure ions overlap with high-density cold plasma increases.

[37] In section 6.1 the findings of the examination of the solar wind and the magnetosphere triggered on relativistic-electron-dropout onsets will be summarized. Many phenomena are approximately simultaneous with the onset of dropouts: the onset of the superdense ion and electron plasma sheet, the onset of the extra-hot ion and electrons plasma sheet, and the onset of plasmaspheric drainage plumes. In section 4.2 these findings will be compared with what is found when the zero epoch is set on the recovery from dropout. That study will hone in on the combination of the superdense ion plasma sheet and the plasmaspheric drainage plumes.

4.2. Triggering on Dropout Recoveries

[38] The superposed average of the data when using the 14 events with sharp recoveries of dropouts and triggering on the steepest part of the recovery in the multisatellite average of the 1.1–1.5 MeV electron flux are displayed in Figures 6 (bottom) and 10i-10r and in the right-hand columns of Figures 7, 8, 9, and 10. The zero epoch (= recovery from dropout) is denoted in each panel of those figures by a vertical dashed line.

[39] The superposed average of the logarithm of the 1.1–1.5 MeV electron flux measured by the multiple satellites around geosynchronous orbit is shown in Figure 5 (bottom), with the zero epoch being the steepest part of the rise in the multisatellite average of the logarithm of the 1.1–1.5 MeV electron flux. Owing to the systematic diurnal trend in the fluxes, it is difficult to see if there is a local-time dependence of the timing of the relativistic-electron flux recovery as plotted in Figure 5. In Figure 6 (bottom), the logarithm of the 1.1–1.5 MeV electron fluxes is averaged over 5 hours of local time centered at midnight (0 LT, red), dawn (6 LT, green), noon (12 LT, blue), and dusk (18 LT, purple) and plotted as functions of time from trigger. The curves from the four local-time regions were fit with hyperbolic-tangents to determine the temporal widths of the recoveries in flux and the relative timing of the recoveries. It is found that the widths of the drops in the four regions vary from 8.3 hr to 12.3 hr. The temporal centers of the recoveries are within 0.75 hours of each other, with the recovery occurring first at midnight, then dusk, then noon, and then dawn. Note, the relative timings determined may not be statistically significant.

[40] In Figure 7h, the superposed average of the logarithm of the multisatellite averaged 1.1–1.5 MeV electron flux at geosynchronous orbit is plotted. The zero epoch (trigger) for the superposition of data is the steepest part of the recovery in the logarithm of the flux. As can be seen, when superposing on the recoveries of the dropouts, the abruptness of the recovery is evident. In Figure 7h, the dropout onset appears gradual owing to the mixed timings of the individual onsets.

[41] In Figures 7i-7l, some solar wind parameters are plotted for triggering on relativistic-electron recoveries. Figure 7i shows the solar wind speed. As can be seen, the recovery from dropout (vertical dashed line) occurs near the end of the interval wherein the solar wind speed is increasing. Figure 7j shows that the recovery occurs in the CIR during the eastward flow deflection of the solar wind. In the superposed average of Figure 7, the recovery (steepest part of the rise) occurs about 10 to 11 hours after the passage of the stream interface (reversal of v_y of the solar wind through zero). Analysis of the individual events that go into the superposed average finds that the recovery occurs 10.5 ± 4.8 hours after the passage of the stream interface. This means that the onset occurs during the passage of the compressed fast wind in the CIR. This is noted in Table 1 and is noted in the CIR sketch of Figure 2. Figure 7k indicates that the recovery occurs after the solar wind density pulse passes. Figure 7l shows that the relativistic-electron recovery from dropout occurs during the fluctuating magnetic field interval of the high-speed stream.

[42] In Figures 7l and 7m, the superposed average of the geomagnetic indices Kp and Dst are displayed, with the data superposition triggered on the relativistic-electron recovery. As can be seen in Figure 7m, the relativistic-electron recovery occurs during the sustained high Kp of the high-speed stream. As can be seen in Figure 7n, the relativistic-electron recovery occurs during the interval when Dst is

balanced between driving and loss. Note that there is no Dst signature corresponding to the relativistic-electron recovery.

[43] In the right-hand column of Figure 8 the density and temperature of the hot ions (ion plasma sheet) and hot electrons (electron plasma sheet and electron trough) around geosynchronous orbit as measured by MPA are shown, with the zero epoch (trigger) of the data superposition being the relativistic-electron recovery. As can be seen in the first and second plots of the right column, the relativistic-electron recovery is approximately simultaneous with the disappearance of the superdense ion plasma sheet and the disappearance of the superdense electron plasma sheet. This is noted in Table 1. As can be seen in Figures 8g and 8h, the extra-hot phase of the ion plasma sheet and the extra-hot phase of the electron plasma sheet both persist beyond the time of recovery of the relativistic electrons. The timing of the relativistic-electron recovery relative to the termination of the superdense plasma sheet will be explored further in Figure 10.

[44] In the right-hand column of Figure 9, some of the properties of the cold-plasma measured around geosynchronous orbit by MPA are shown, with the zero epoch (trigger) of the data superposition being the relativistic-electron recovery. Figure 9e shows the superposed average of the cold-plasma density. At the time of relativistic-electron recovery, the drainage plume appears to weaken substantially in terms of plasma number density. This same phenomena is seen again in Figure 9f, where the fraction of time that the cold-plasma density is observed to be above 10 cm^{-3} is shown. Looking statistically at the properties of plasmaspheric drainage plumes during high-speed-stream-driven storms (without selection as to whether or not there was a relativistic-electron dropout or recovery), *Borovsky and Denton* [2008] found that the average number density n_{ave} of plume plasma decays with time as $n_{ave} \propto \exp(-t/78$ hours). The local-time widths W of the plumes were also found to decrease with time t from storm onset. If the product Wn_{ave} in that plume data set is fit, then a temporal decay of the form exp(−t/44 hours) is obtained. The plume properties in Figure 9 appear to decay faster than a 44-hr e-folding time. In Figure 9g, the superposed average of the flow speed of the cold-plasma measured at geosynchronous orbit is shown. No clear signature in the cold-plasma flow properties is seen in correlation with the time of relativistic-electron dropout. In Figure 9h, the superposed average of the product of the hot-ion pressure (in units of nPa) and the cold-ion density (in units of cm^{-3}) is plotted. Note that the color scale is logarithmic. This plot shows the regions where there is strong potential for the growth of electromagnetic ion-cyclotron (EMIC) waves: sufficient free energy in the hot ions and sufficient cold plasma. As can be seen, this product drops noticeably at the time of relativistic-electron recovery.

[45] In the right-hand column of Figure 10 we will look for indications of what causes the recovery from the relativistic-electron dropouts. To guide the eye, in each panel of the right-hand column the multisatellite average of the logarithm of the 1.1–1.5 MeV electron flux triggered on the dropout recovery is drawn in gray, and the trigger is drawn as the vertical dashed line. In Figures 10j to 10l, the orbit-averaged density, temperature, and pressure of the ion plasma sheet is plotted. As can be seen in Figures 10j to 10l, the recovery of the relativistic-electron flux is not associated with the hot-ion temperature and the recovery is weakly associated with the hot-ion density and pressure. In Figures 10m to 10o, the orbit-averaged density, temperature, and pressure of the hot electrons is plotted. Likewise, the recovery of the relativistic-electron flux is not associated with the hot-electron temperature and the recovery is weakly associated with the hot-electron density and pressure. In Figures 10p and 10q, the orbit-averaged cold-ion density and the cold-ion flow velocity averaged over the 14–18 LT regime are plotted. The recovery from relativistic-electron dropout is associated with the decay of the orbit-averaged cold-ion density but is not associated with the cold-ion velocity. The decay of the orbit-averaged density is a indication that the plasmaspheric drainage plumes are getting less dense and narrower with age [cf. *Borovsky and Denton*, 2008]. Finally, in Figure 10r, the fraction of time over the geosynchronous orbit that both the cold-ion density is greater then 10 cm^{-3} and the hot-ion pressure is greater then 1 nPa is plotted. As can be seen, simultaneous with the recovery from the relativistic-electron dropout the fraction of time high-pressure ions overlap with high-density cold plasma decreases.

[46] The key finding of this subsection and the last appears to be the association of the relativistic-electron dropout with the combined superdense ion plasma sheet and the plasmaspheric drainage plume. In particular, dropouts occur when the superdense ion plasma sheet spatially overlaps the drainage plume.

4.3. Events Without Dropouts

[47] To test some of the findings of the previous two subsections, a set of 10 events is collected wherein no relativistic-electron dropout nor recovery occur. Those events are analyzed in Figures 11 and 12. Since there are neither onsets nor recoveries, the superposed epoch is triggered on the onset of convection in the storm, as was the triggering in Figures 3 and 4.

[48] In Figure 11a, the superposed average of the logarithm of the multisatellite-averaged 1.1–1.5 MeV electron flux is plotted. Note that no relativistic-electron dropout is seen. This is in contrast with Figure 3 (top) where the triggering is the same but clear dropouts in the relativistic-electron flux are seen in the superposed averages. In Figures 11b-11e, superposed averages of the solar wind parameters are plotted. As can be seen in Figures 11c and 11d, the CIR signatures are weak: the magnitude of the east-west shear flow is modest (Figure 11c) and the solar wind-density perturbation is very weak (Figure 11d). Figure 11e indicates that the B_z (GSM) signature is also modest.

[49] In Figures 11f and 11g, the superposed averages of the Kp and Dst indices are displayed. The superposed average of Kp indicates a weak onset of convection, whilst the Dst perturbation of the storm is also very weak.

[50] In Figure 12 the superposed averages of the properties of the hot and cold plasmas around geosynchronous orbit as measured by MPA are shown. Figures 12a and 12e contain the density and temperature of the ion plasma sheet. Although the ion plasma sheet goes into a extra-hot phase at the time of storm onset (Figure 12e), it does not go into a superdense phase (Figure 12a). Similarly for the superposed averages of the electron plasma sheet in the second row of

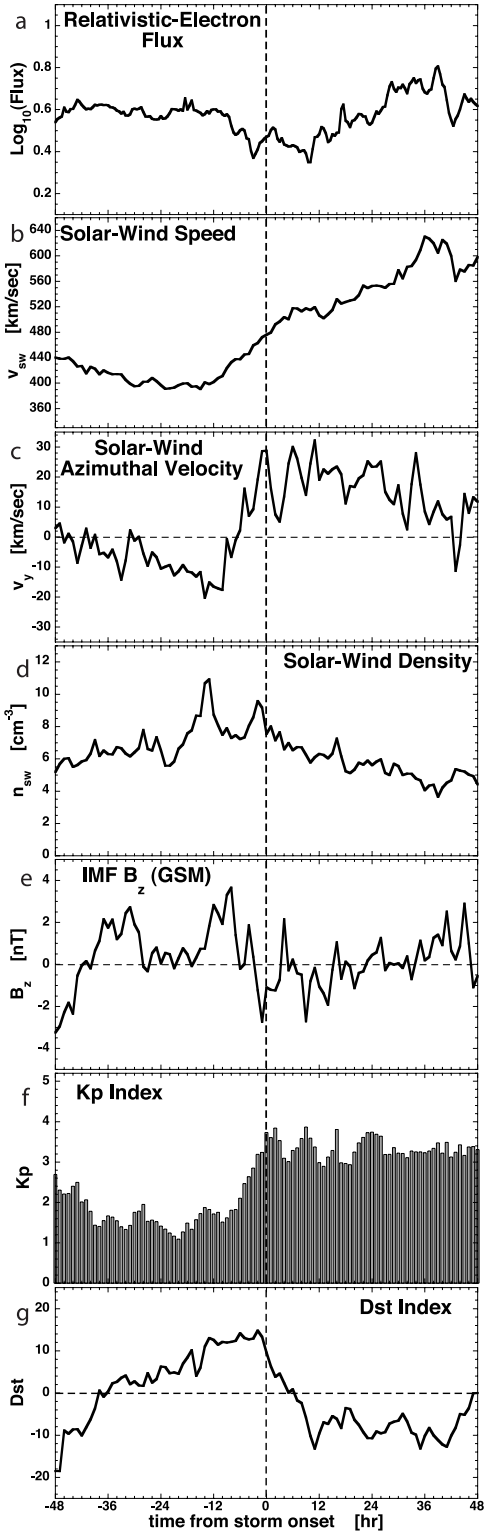

Figure 11. For a set of 10 storms that had neither dropouts nor recovery, superpositions of several measurements are plotted. (a) Logarithm of the multisatellite average of the 1.1–1.5 MeV electron flux at geosynchronous orbit. (b) Solar wind speed. (c) Solar wind azimuthal (east-west or ecliptic) flow velocity. (d) Solar wind number density. (e) z-Component (GSM) of the solar wind magnetic field. (f) Kp index. (g) Dst index. The trigger for the data superposition is the onset of storm levels of convection in the magnetosphere.

Figure 11: a extra-hot phase occurs associated with the onset of the storm but no superdense phase is seen. In the third row of Figure 11 the superposed averages of the cold ion density and occurrence probability are shown. In Figure 12c, the formation of a plasmaspheric drainage plume in the post-noon sector can be seen at storm onset, but weak. The occurrence probability (fraction of time the cold-plasma density is above 10 cm^{-3}) in Figure 12g shows a similar behavior.

[51] Figure 11g shows the logarithm of the 1.1–1.5 MeV electron flux measured by SOPA on multiple satellites around geosynchronous orbit. No clear dropout is seen and no sharp recovery is seen. Note however that the relativistic-electron fluxes do slowly increase as the storm progresses (see also Figure 11a).

[52] From this examination of events without dropouts, it is found that there is no high-density pulse in the solar wind and hence no superdense plasma sheet in the magnetosphere. There are drainage plumes, but weak.

5. Implications of the Findings

[53] From the examination of the temporal association of the solar wind and magnetosphere with the onset and recovery of relativistic-electron dropouts in section 4, it appears that dropouts are caused by the combination of a superdense plasma sheet and a plasmaspheric drainage plume. The scenario envisioned is that these two phenomena act in concert to produce EMIC waves which pitch-angle scatter the relativistic electrons into the atmospheric loss cone. About 6 hours of scattering is required to deplete the 1.1–1.5 MeV relativistic-electron population at geosynchronous orbit and the population stays depleted for about 6–20 hours.

[54] The cause for the dropout being the overlap of the superdense plasma sheet and the plasmaspheric drainage plume is explored further in Figures 13 and 14. In Figures 13a to 13c, the fraction of time that the cold-ion density is greater then 10 cm^{-3} and simultaneously the hot-ion pressure is greater then 1 nPa is plotted. In Figure 13a, the trigger is on the onset of relativistic-electron dropout and in Figure 13b, the trigger is on the recovery. As can be seen, at about the time of trigger (Figure 13a) the fraction of time that there is overlap between a superdense plasma sheet and a drainage plume is significant, 50% or greater at the afternoon local-time regions where plumes are expected. In addition, as can be seen, at about the time of recovery (Figure 13b) this high probability diminishes significantly. When there is no dropout nor recovery (Figure 13c), the probability of an overlap of high-pressure plasma sheet with cold ions is lower. This can be seen in Figure 13d where the probabilities of Figures 13a to 13c are averaged over local time. An example of this is shown in Figure 14, where the interplay of the plasmaspheric drainage plume (blue), the ion plasma sheet (red), and the relativistic-electron dropout (green) as seen by the spacecraft 1989–046 in geosynchronous orbit during the November 1993 National Space Weather Program Storm [*Knipp et al.*, 1998] is shown. (See *Borovsky et al.* [1998a] for a fuller analysis of this event.) The green curve (right axis) plots the 1.1–1.5 MeV electron flux as measured by the SOPA instrument on board the spacecraft 1989–046 for 5.5 days in November 1993.

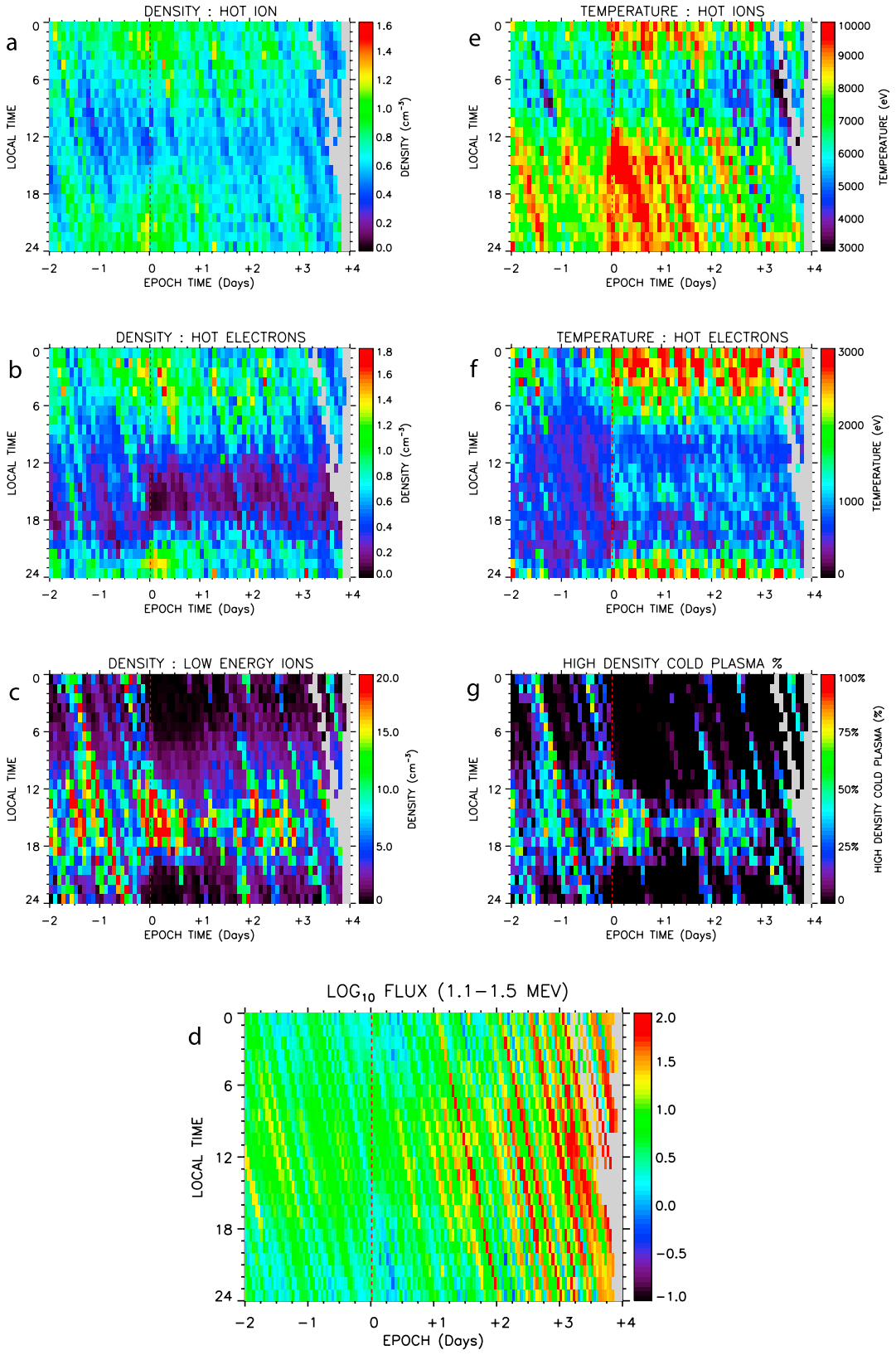

Figure 12. For 10 events without dropouts or recoveries, superpositions of several measurements are plotted. (a) Density and temperature of the hot ions (0.1–45 keV) around geosynchronous orbit. (b) Density and temperature of the hot electrons (0.03–45 keV) around geosynchronous orbit. (c) Number density of the cold ions (1–100 eV) around geosynchronous orbit and the fraction of time that that density is measured to be greater than 10 cm^{-3}. (d) Logarithm of the flux of 1.1–1.5 MeV electrons around geosynchronous orbit.

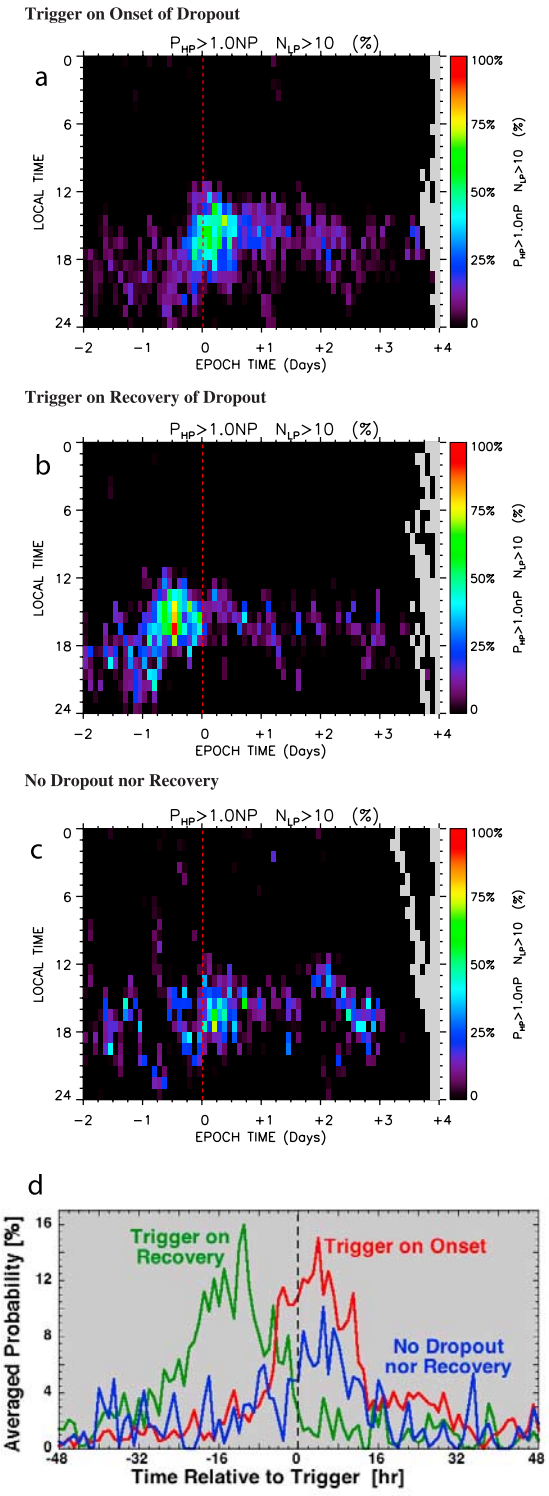

Figure 13. The fraction of time that the hot-ion (0.1–45 keV) pressure is greater than 1 nPa at the same time that the cold-ion (1–100 eV) density is greater than 10 cm^{-3} is compared around geosynchronous orbit. (a) Quantity is plotted triggered on the onset of relativistic-electron dropout (for 33 events with clear onsets). (b) Quantity is plotted triggered on dropout recovery (for 14 events with clear recoveries). (c) Quantity is plotted triggered on storm-convection onset for 10 events that have neither dropout nor recovery. (d) The probabilities are averaged over local time.

The relativistic-electron dropout (labeled) begins just before midnight of 3–4 November and ends just after midday on 4 November. During this dropout, the spacecraft 1989–046 makes one crossing of the drainage plume in the afternoon sector. The cold-plasma number density as measured by the MPA detector on 1989–046 is plotted in blue (left axis) and this first plume crossing early on 4 November is labeled in Figure 14. The hot-ion pressure in the energy range 100 eV to 40 keV as measured by MPA onboard 1989–046 is plotted in red (right axis). As can be seen, during this first plume crossing the pressure of the ion plasma sheet within the plume was 2 nPa or higher. As noted in the study by *Borovsky et al.* [1998a], the plasma sheet was in a superdense phase during this first plume crossing on 4 November. During this geomagnetic storm, the spacecraft 1989–046 crossed through the drainage plume several more times, once per day. The next four plume crossings are shown in blue and are labeled in Figure 14. The green curve demonstrates that those subsequent plume crossings were after the relativistic-electron dropout had recovered. As can be seen from the red curve, the pressure of the ion plasma sheet inside the plume was low on the crossings after the dropout had recovered. The plume was still there, but the plasma sheet was not superdense.

[55] The superdense ion plasma sheet is produced by the entry of the high-density solar wind of the CIR into the Earth's magnetosphere with about a 2- to 8-hour time lag [*Denton and Borovsky*, 2008b]. The high-density solar wind that produces the superdense plasma sheet is mainly compressed slow wind ahead of the CIR stream interface.

[56] The plasmaspheric drainage plume is the result of strong convection in the magnetosphere. The onset of convection comes from the southward (GSM) IMF after the passage of the IMF sector reversal, with the sector reversal typically passing the Earth prior to the passage of the CIR stream interface. The GSM southward IMF comes about from the Parker-spiral-like magnetic field of the CIR owing to a Russell-McPherron effect [*Russell and McPherron*, 1973]. Because of this Russell-McPherron effect, there are more high-speed-stream-driven storms in the Spring and Fall than there are in the Summer and Winter [cf. *Crooker and Cliver*, 1994; *Mursula and Zieger*, 1996; *McPherron and Weygand*, 2006; *Borovsky and Steinberg*, 2006]. Of the 124 storms studied in section 3, 56% occurred in Spring and Fall and 44% occurred in Summer and Winter, and of the 33 clean dropout events studied in section 4, 58% occurred in Spring and Fall and 42% occurred in Summer and Winter.

[57] As an aside, note that a complementary region of overlap between the superdense electron plasma sheet and high-density cold plasma is not expected. The electron plasma sheet tends not to overlap spatially with plasmaspheric material [*Horwitz et al.*, 1986; *Moldwin et al.*, 1995; *Denton et al.*, 2005]. As a check on this, the product of the hot-electron pressure with the cold-ion density is calculated and found to be on average two orders of magnitude lower than the product of the hot-ion pressure with the cold-ion density.

[58] As stated above, it appears that relativistic-electron dropouts are caused by the combination of a superdense plasma sheet and a plasmaspheric drainage plume. It is well known that EMIC waves grow best in locations where the

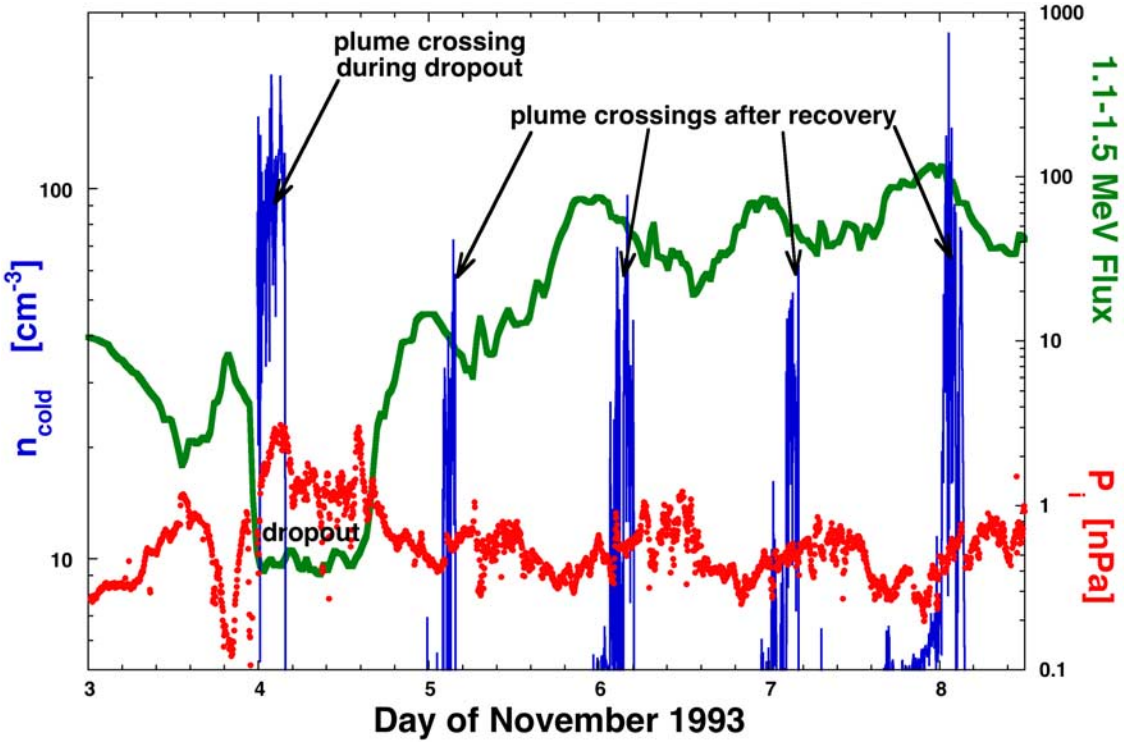

Figure 14. For a high-speed-stream-driven storm in November 1993, the cold-plasma (1–100 eV) density (blue, left axis), the hot-ion (0.0–45 keV) pressure (red, right axis), and the logarithm of the 1.1–1.5 MeV electron flux (green, right axis) are all plotted measured onboard the spacecraft 1989-046 in geosynchronous orbit. The pressure of the ion plasmas sheet inside the plasmaspheric drainage plume can be compared for a plume during the relativistic-electron dropout versus plumes after the recovery from dropout.

hot ions of the magnetosphere drive the waves and the cold plasma of the magnetosphere reduces the instability threshold [e.g., *Cornwall et al.*, 1970; *Fraser and Nguyen*, 2001; *Meredith et al.*, 2003; *Fuselier et al.*, 2004]. EMIC waves have been theoretically expected to grow in drainage plumes [e.g., *Kovalevskiy*, 1980, 1981; *Jordanova et al.*, 2006; *Thorne et al.*, 2006] and there is indirect evidence for EMIC waves scattering particles from plume regions [e.g., *Spasojevic et al.*, 2004; *Fraser et al.*, 2006; *Yahnin and Yahnina*, 2007; *Jordanova et al.*, 2007]. With the large amount of free energy in the superdense, extra-hot ion plasma sheet, this makes the regions where the superdense ion plasma sheet penetrates into the plasmaspheric drainage plumes very likely regions for EMIC-wave growth. EMIC waves can be powerful sources of pitch-angle scattering of relativistic electrons into the atmospheric loss cone [e.g., *Thorne and Kennel*, 1971; *Horne and Thorne*, 1998; *Summers et al.*, 1998; *Summers and Thorne*, 2003; *Sandanger et al.*, 2007]. The high density of the drainage plume also lowers the resonance energy for interaction of the EMIC waves with the relativistic electrons of the radiation belt [cf. *Thorne and Kennel*, 1971; *Summers and Thorne*, 2003; *Meredith et al.*, 2003]. This makes the regions where the superdense ion plasma sheet penetrates into the plasmaspheric drainage plumes very likely regions for relativistic-electron scattering. Note that plasmaspheric drainage plumes extend across all L shells of the dayside magnetosphere from the storm-time-contracted plasmapause all the way to the magnetopause [*Elphic et al.*, 1996; *Borovsky et al.*, 1997; *Su et al.*, 2000; *Goldstein et al.*, 2004]. Because of this extension, there is potentially a region of favorable wave growth and favorable relativistic-electron scattering at all L shells.

[59] We suggest that two other factors that may enhance the favorability of those superdense-plasma-sheet/drainage-plume overlap regions for strong EMIC growth: (1) the strong density gradients in the lumpy drainage plumes increases the ducting of EMIC waves and (2) "energy-pitch-angle dark lanes" in the dayside ion-plasma-sheet distribution functions increase the free energy for wave growth. These two factors are discussed in the next two paragraphs.

[60] Plasmaspheric drainage plumes are lumpy [*Taylor et al.*, 1970; *Spasojevic et al.*, 2003; *Moldwin et al.*, 2004; *Goldstein et al.*, 2004]. As soon as plasmaspheric plasma begins to convect at the onset of a storm, the lumpiness of the plasma is observed to increase greatly [*Borovsky and Denton*, 2008]. Using 10-second snapshots of the plasma number density made every 86 seconds, the fractional variance $\delta n/n = 2(n_2 - n_1)/(n_1 + n_2)$ of drainage-plume plasma density was analyzed by *Borovsky and Denton* [2008], where n_1 and n_2 are two sequential measurements of the density separated by 86 seconds. For 470 hours of measurements in drainage plumes, the mean value of $\delta n/n$ was found to be 0.57. With cold-plasma convection velocities of ~15 km/sec, the 86-sec cadence of the measurements

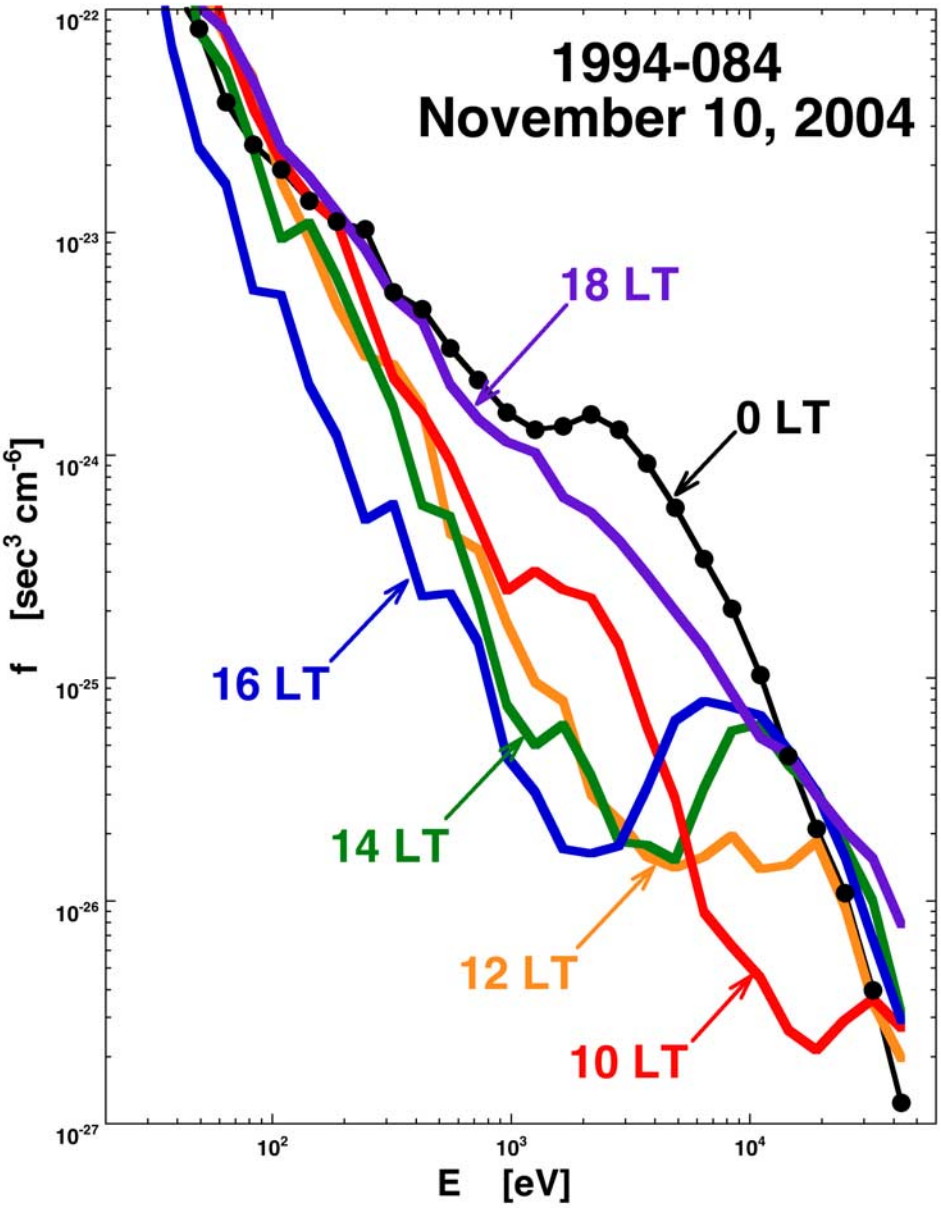

Figure 15. As measured by the MPA instrument onboard the spacecraft 1994-084 in geosynchronous orbit, several ion energy distribution functions are shown for the day of 10 November 2004. As the spacecraft crossed the dayside magnetosphere that day, the relativistic-electron fluxes were dropping out. From 13 to 18 LT, the spacecraft 1994-084 was in a plasmaspheric drainage plume. The distributions at 14 LT, 16 LT, and 18 LT are for superdense plasma sheets within plasmaspheric drainage plumes with $P_i > 1$ nPa and $n_{cold} > 10$ cm^{-3}.

corresponded to ~1300 km of distance transverse to the magnetic field, so the plumes are filled with strong density gradients with gradient scales on the order of 1000 km. It is well known that ducting along field-aligned density structures enhances the growth of EMIC waves [*Thorne and Horne*, 1997; *Fraser and Nguyen*, 2001; *Khazanov et al.*, 2006] and the lumpiness of plumes should provide broad regions where the EMIC growth is enhanced: not just at the plume edges, but throughout the plume interiors.

[61] The ion distribution functions in the dayside magnetosphere are very structured. As the ions of the plasma sheet are transported from the nightside magnetosphere to the dayside, ions with different kinetic energies and different pitch angles follow different trajectories around the dipole [e.g., *Ejiri et al.*, 1980; *Greenspan et al.*, 1985; *Ebihara and Ejiri*, 2002]. Some ions pass around the dawn side of the Earth and some pass around the dusk side. The energy/pitch-angle ion distribution function observed at any location in the dayside magnetosphere is an assemblage of ions that have come from the nightside along these various pathways around the dipole. The various paths carry the ions through different depths of the hydrogen geocorona around the Earth. The hydrogen geocorona acts to remove ions by charge exchange. Passing to different depths in the

geocorona means that the attenuation factor for ions differs on the differing pathways to the dayside. Additionally, ions with different pitch angles mirror at different depths in the geocorona. As a result of the differing loss rates, there are lanes of missing ions in the assembled distribution functions on the dayside where various energies and pitch angles suffered heavy attenuation from the geocorona [cf. *Kistler et al.*, 1989, 1999; *Jordanova et al.*, 1999]. An example is shown in Figure 15. Here five omni-directional ion distribution functions measured at various local times across the dayside magnetosphere by the MPA instrument on the spacecraft 1994-084 on 10 November 2004 are shown, with one measured at local midnight (black) for comparison. As the spacecraft 1994-084 moved across the dayside magnetosphere on 10 November 2004, the 1.1–1.5 MeV electrons at geosynchronous orbit were dropping out. When the distributions at 14 LT (green), 16 LT (blue), and 18 LT (purple) in Figure 15 were measured, the spacecraft was simultaneously in the superdense ion plasma sheet (with hot-ion pressure greater than 1 nPa) and the plasmaspheric drainage plume (with cold-ion density greater than 10 cm^{-3}) while the relativistic electrons were dropping out. As can be seen in Figure 15, the ion distribution functions in the dayside magnetosphere are not monotonic. The detailed structure is caused by a combination of temporal source populations, time-dependent convection, and shadowing by the geocorona [cf. *Mauk and Meng*, 1983; *Maurice et al.*, 1998; *Korth et al.*, 2002]. The driving of EMIC waves by a geocorona-produced temperature anisotropy of the dayside ion plasma sheet has been explored [e.g., *Cornwall*, 1977; *Solomon and Picon*, 1981]; we suggest further that local regions of $\partial f/\partial v_\perp$ produced by geocorona shadowing may also play a role in EMIC growth [see also *Kaye et al.*, 1979].

[62] To summarize, five things conspire to produce strong EMIC wave growth and effective relativistic-electron scattering to produce the relativistic-electron dropouts.

[63] 1. The ion plasma sheet becomes superdense owing to the high-density compressed slow wind of the CIR, and this increases the free energy content of the plasma-sheet ions.

[64] 2. The superdense plasma sheet is extra-hot owing to the vfast solar wind speed, which produces a hot magnetosheath behind the bow shock, and this extra-hot plasma sheet has more free energy.

[65] 3. The cold plasma of the plasmaspheric drainage plume is very lumpy, providing a medium in which ducting of EMIC waves yields better wave growth.

[66] 4. The plasmaspheric drainage plumes extend across all dayside L shells from the plasmapause to the magnetopause, providing a medium for EMIC waves that can pitch-angle scatter radiation-belt particles at all L shells.

[67] 5. The dark lanes in the distribution functions of the dayside ion plasma sheet may provide localized regions of $\partial f/\partial v_\perp$ which may provide free energy in addition to temperature anisotropy to drive the growth of EMIC waves.

[68] Other mechanisms for eliminating relativistic electrons from the magnetosphere have been proposed, including pitch-angle scattering by plasmaspheric hiss inside the plasmasphere [e.g., *Thorne et al.*, 1979; *Horne et al.*, 2003; *Meredith et al.*, 2004], pitch-angle scattering by whistler-mode chorus waves outside the plasmasphere [e.g., *Tsurutani and Smith*, 1974, 1977; *Summers et al.*, 1998, 2004; *Smith et al.*, 2004; *Albert*, 2005], the Dst effect [e.g., *Dessler and Karplus*, 1961; *Kim and Chan*, 1997], magnetopause shadowing [e.g., *West et al.*, 1972; *Li et al.*, 1997; *Desorgher et al.*, 2000; *Bortnik et al.*, 2006], and outward radial diffusion [e.g., *Brautigam and Albert*, 2000; *Shprits et al.*, 2006]. These other mechanisms may play a role, but our findings indicate that scattering by EMIC waves is the primary candidate for the dropout loss mechanism.

[69] As we have seen in section 4.2, recovery of the relativistic-electron dropouts is associated with the decay of the density and local-time width of plasmaspheric drainage plumes and with the superdense plasma sheet becoming an ordinary-density plasma sheet. That is, recovery of the relativistic-electron dropout is associated with a turnoff of the strong EMIC growth region. Questions arise: Why don't the relativistic-electron fluxes (and relativistic-electron number densities) stay low after the EMIC growth is shut off? Why do the relativistic-electron fluxes (and the relativistic-electron densities: see Figure 1) increase rapidly when the EMIC scattering ceases? This will be the subject of a future study. It is clear that there is more to discover about the recovery of relativistic-electron dropouts.

6. Summary of Findings, Conclusions About Dropouts, and Future Work

[70] In sections 6.1, 6.2, and 6.3 the detailed findings about the onsets of relativistic-electron dropout, about the recoveries of relativistic-electron dropouts, and about the absences of relativistic-electron dropouts are summarized. Much of that summary is incorporated into Table 1. In section 6.4 the major conclusions about the cause of relativistic-electron dropouts are stated. Finally, future research that is needed is described in section 6.5.

6.1. Findings About Dropout Onsets

[71] In section 4.1 superposed epoch studies of the solar wind and the magnetosphere were performed with the trigger for the data alignment being the onset of relativistic-electron dropouts at geosynchronous orbit. The findings of those studies are the following:

[72] 1. Dropout onsets are nearly simultaneous at all local times. Detailed fits to the superposed average of the logarithm of the 1.1–1.5 MeV electron flux indicate that the dropout commences first at dawn, then at midnight, then at dusk, and then at noon.

[73] 2. At geosynchronous orbit, the 1.1–1.5 MeV electrons require about 6 hours to fully drop out.

[74] 3. The onset of relativistic-electron dropout occurs during the passage of the compressed slow wind of the CIR, after the passage of the sector reversal and before the passage of the stream interface.

[75] 4. The onset of the relativistic-electron dropout is simultaneous with the peak westward solar wind deflection of the CIR at the beginning of the solar wind-speed ramp.

[76] 5. The onset of relativistic-electron dropout occurs at the time of onset of the storm convection as measured by the strong rise of the Kp index.

[77] 6. The onset of the relativistic-electron dropout occurs while the Dst index is falling.

[78] 7. The onset of the relativistic-electron dropout occurs at same time as drainage-plume formation.

[79] 8. The onset of the relativistic-electron dropout occurs at same time as the onset of the superdense ion plasma sheet.

[80] 9. The onset of the relativistic-electron dropout occurs at same time as the onset of the extra-hot phase of ion plasma sheet.

[81] 10. The onset of relativistic-electron dropout occurs at same time as the onset of the superdense electron plasma sheet.

[82] 11. The onset of relativistic-electron dropout occurs at the same time as the onset of the extra-hot phase of electron plasma sheet.

[83] 12. The onset of relativistic-electron dropout occurs when there is significant overlap of the superdense ion plasma sheet with the plasmaspheric drainage plume.

6.2. Findings About Dropout Recoveries

[84] In section 4.2 superposed epoch studies of the solar wind and the magnetosphere were performed with the trigger for the data alignment being the recovery of relativistic-electron dropouts at geosynchronous orbit. The findings of those studies are the following:

[85] 1. The 1.1–1.5 MeV electron-dropout recovery at geosynchronous orbit begins almost simultaneously at all local times: detailed fits to the superposed average of the logarithm of the 1.1–1.5 MeV electron flux indicate that the dropout commences first at midnight, then dusk, then noon, and then dawn.

[86] 2. At geosynchronous orbit the 1.1–1.5 MeV electrons require about 12–18 hours to recover.

[87] 3. The flux of 1.1–1.5 MeV electrons at geosynchronous orbit can be either higher or lower immediately after recovery than before dropout.

[88] 4. The relativistic-electron number density at geosynchronous orbit tends to be higher immediately after recovery than it was before dropout.

[89] 5. The relativistic-electron-dropout recovery occurs during the passage of the compressed fast wind of the CIR, after the passage of the stream interface.

[90] 6. The relativistic-electron-dropout recovery ramp extends beyond the end of the CIR into the undisturbed fast wind. I.e. full recovery occurs when the fast wind after the CIR is passing.

[91] 7. The relativistic-electron-dropout recovery is not associated with any change in the Kp or Dst indices.

[92] 8. The relativistic-electron-dropout recovery occurs at same time as a strong decay in the properties of the plasmaspheric drainage plume.

[93] 9. The relativistic-electron-dropout recovery occurs during the slow decay of the superdense ion plasma sheet to ordinary densities.

[94] 10. The relativistic-electron-dropout recovery is not associated with a change in extra-hot phase of ion plasma sheet. The extra-hot phase continues long after the dropout recovers.

[95] 11. The relativistic-electron-dropout recovery occurs during the slow decay of the superdense electron plasma sheet to ordinary densities.

[96] 12. The relativistic-electron-dropout recovery is not associated with a change in extra-hot phase of electron plasma sheet. The extra-hot phase continues long after the dropout recovers.

[97] 13. The relativistic-electron-dropout recovery occurs when the significant overlap between the superdense ion plasma sheet and the drainage plume ends.

6.3. Findings About the Absence of Dropouts

[98] In section 4.3 superposed epoch studies of the solar wind and the magnetosphere were performed for storms that had neither relativistic-electron dropout nor recovery, with the trigger for the data alignment being the onset of storm levels of magnetospheric convection. The findings of those studies are the following:

[99] 1. When there is no relativistic-electron dropout, no superdense ion plasma sheet occurs.

[100] 2. When there is no relativistic-electron dropout, no superdense electron plasma sheet occurs.

[101] 3. When there is no relativistic-electron dropout, drainage plumes still form, but the plumes are weak.

[102] 4. When there is no relativistic-electron dropout, the extra-hot phase of the ion plasma sheet still occurs.

[103] 5. When there is no relativistic-electron dropout, the extra-hot phase of the electron plasma sheet still occurs.

6.4. Conclusions About Relativistic-Electron Dropouts

[104] From the examination of the magnetosphere phased with the onsets and recoveries of relativistic-electron dropouts, it appears that dropouts are caused by the combination of a superdense plasma sheet and a plasmaspheric drainage plume. The scenario envisioned is that when the superdense ion plasma sheet spatially overlaps the plasmaspheric drainage plume, the two phenomena act in concert to produce EMIC waves which pitch-angle scatter the relativistic electrons into the atmospheric loss cone. About 6 hours of scattering is required to deplete the 1.1–1.5 MeV relativistic-electron population at geosynchronous orbit, the population stays depleted for about 6–20 hours, and the recovery of the fluxes take about 12–18 hours.

[105] The origin of the superdense plasma sheet is the compressed slow wind of the CIR ahead of the stream interface. This high-density plasma enters into the magnetosphere with about a 2–8 hour time lag to produce the superdense plasma sheet at geosynchronous orbit.

[106] The origin of the plasmaspheric drainage plume is the enhanced magnetospheric convection associated with southward (GSM) solar wind magnetic field after the passage of the IMF sector reversal prior to the passage of the CIR stream interface.

[107] For storms without relativistic-electron dropouts, superdense plasma sheets are not present.

6.5. Future Work Needed

[108] The relativistic-electron dropouts investigated in the present study all occurred during high-speed-stream-driven storms. Relativistic-electron dropouts also need to be studied in CME-driven storms. Because the CME-driven storms are more variable than are high-speed-stream-driven storms, the dropouts or lack of dropouts under more-varying conditions can be studied. In particular, CME-driven storms with plasmaspheric drainage plumes but without superdense plasma sheets (or vice versa) will be of great interest to confirm or modify the conclusions of the present study.

[109] It has been suggested here that the plentiful density gradients within plasmaspheric drainage plumes may be of importance for the ducting of EMIC waves and the improvement of their growth. The lumpiness of plasmaspheric drainage plumes needs to be studied and quantified with higher-resolution plasma measurements to enable a better theoretical assessment of the impact of the lumpiness on the EMIC wave growth.

[110] It has also been suggested here that the lanes of missing ions in the three-dimensional ion distribution functions may provide an additional source of free energy (i.e. $\partial f/\partial v_\perp$) for the growth of EMIC waves in the dayside magnetosphere. A survey of the properties of the ion distribution functions of the dayside magnetosphere is called for and a theoretical assessment of their importance for EMIC wave growth should be performed.

[111] Finally, when the relativistic-electron flux recovers from a dropout, the relativistic-electron number density immediately after the recovery can have a considerable range of values. This number density represents a fundamental measure of the new population of electrons that are available in the subsequent days of the storm to be heated to produce the several-day-long increase in the relativistic-electron fluxes through the storm [cf. *Borovsky et al.*, 1998a]. Learning what factors determine the density of relativistic electrons when they enter the outer dipole at recovery will be important for determining the ultimate level of relativistic-electron fluxes late in the storm.

[112] **Acknowledgments.** The authors thank John Steinberg for useful conversations and Reiner Friedel for SOPA data, Tom Cayton for fits to the SOPA data, Bob McPherron for his list of solar wind stream interfaces, and Michelle Thomsen for MPA data. J.E.B. thanks the Department of Communication Systems at Lancaster University for their hospitality. This research was supported by the NASA Targeted Research and Technology Program, by the NSF National Space Weather Program, and by the Los Alamos National Laboratory LDRD Program.

[113] Amitava Bhattacharjee thanks Nigel Meredith and another reviewer for their assistance in evaluating this paper.

References

Albert, J. M. (2005), Evaluation of quasi-linear diffusion coefficients for whistler mode waves in a plasma with arbitrary density ratio, *J. Geophys. Res.*, *110*, A03218, doi:10.1029/2004JA010844.

Baker, D. N., and R. L. McPherron (1990), Extreme energetic particle decreases near geosynchronous orbit: A manifestation of current diversion within the inner plasma sheet, *J. Geophys. Res.*, *95*, 6591.

Bame, S. J., D. J. McComas, M. F. Thomsen, B. L. Barraclough, R. C. Elphic, J. P. Glore, J. T. Gosling, J. C. Chavez, E. P. Evans, and F. J. Wymer (1993), Magnetospheric plasma analyzer for spacecraft with constrained resources, *Rev. Sci. Instrum.*, *64*, 1026.

Belian, R. D., G. R. Gisler, T. Cayton, and R. Christensen (1992), High-Z energetic particles at geosynchronous orbit during the great solar proton event series of October 1989, *J. Geophys. Res.*, *97*, 16,897.

Blake, J. B., R. S. Selesnick, D. N. Baker, and S. Danekal (2001), Studies of relativistic electron injection events in 1997 and 1998, *J. Geophys. Res.*, *106*, 19,157.

Bogott, F. H., and F. S. Mozer (1973), Nightside energetic particle decreases at the synchronous orbit, *J. Geophys. Res.*, *78*, 8119.

Borovsky, J. E., and M. H. Denton (2006), The differences between CME-driven storms and CIR-driven storms, *J. Geophys. Res.*, *111*, A07S08, doi:10.1029/2005JA011447.

Borovsky, J. E., and M. H. Denton (2008), A statistical look at plasmaspheric drainage plume, *J. Geophys. Res.*, *113*, A09221, doi:10.1029/2007JA012994.

Borovsky, J. E., and J. T. Steinberg (2006), The "calm before the storm" in CIR/magnetosphere interactions: Occurrence statistics, solar-wind statistics, and magnetospheric preconditioning, *J. Geophys. Res.*, *111*, A07S10, doi:10.1029/2005JA011397.

Borovsky, J. E., M. F. Thomsen, and D. J. McComas (1997), The superdense plasma sheet: Plasmaspheric origin, solar-wind origin, or ionospheric origin?, *J. Geophys. Res.*, *102*, 22,089.

Borovsky, J. E., M. F. Thomsen, D. J. McComas, T. E. Cayton, and D. J. Knipp (1998a), Magnetospheric dynamics and mass flow during the November 1993 storm, *J. Geophys. Res.*, *103*, 26,373.

Borovsky, J. E., M. F. Thomsen, and R. C. Elphic (1998b), The driving of the plasma sheet by the solar wind, *J. Geophys. Res.*, *103*, 17,617.

Bortnik, J., R. M. Thorne, T. P. O'Brien, J. C. Green, R. J. Strangeway, Y. Y. Shprits, and D. N. Baker (2006), Observation of two distinct, rapid loss mechanisms during the 20 November 2003 radiation belt dropout event, *J. Geophys. Res.*, *111*, A12216, doi:10.1029/2006JA011802.

Brautigam, D. H., and J. M. Albert (2000), Radial diffusion analysis of outer radiation belt electrons during the October 9, 1990, magnetic storm, *J. Geophys. Res.*, *105*, 291.

Burlaga, L. F. (1974), Interplanetary stream interfaces, *J. Geophys. Res.*, *79*, 3717.

Burlaga, L. F., and R. P. Lepping (1977), The causes of recurrent geomagnetic storms, *Planet. Space Sci.*, *25*, 1151.

Carpenter, D. L., B. L. Giles, C. R. Chappell, P. M. E. Decreau, R. R. Anderson, A. M. Persoon, A. J. Smith, Y. Corcuff, and P. Canu (1993), Plasmasphere dynamics in the duskside bulge region: A new look at an old topic, *J. Geophys. Res.*, *98*, 19,243.

Cayton, T. E., R. D. Belian, S. P. Garyt, T. A. Fritz, and D. N. Baker (1989), Energetic electron components at geosynchronous orbit, *Geophys. Res. Lett.*, *16*, 147.

Chappell, C. R. (1974), Detached plasma regions in the magnetosphere, *J. Geophys. Res.*, *79*, 1861.

Chappell, C. R., K. K. Harris, and G. W. Sharp (1970), The morphology of the bulge region of the plasmasphere, *J. Geophys. Res.*, *75*, 3848.

Chen, A. J., and J. M. Grebowsky (1974), Plasma tail interpretations of pronounced detached plasma regions measured by Ogo 5, *J. Geophys. Res.*, *79*, 3851.

Cornwall, J. M. (1977), On the role of charge exchange in generating unstable waves in the ring current, *J. Geophys. Res.*, *82*, 1188.

Cornwall, J. M., F. V. Coroniti, and R. M. Thorne (1970), Turbulent loss of ring current protons, *J. Geophys. Res.*, *75*, 4699.

Crooker, N. U., and E. W. Cliver (1994), Postmodern view of M-regions, *J. Geophys. Res.*, *99*, 23,383.

Denton, M. H., and J. E. Borovsky (2008a), Superposed epoch analysis of high-speed-stream effects at geosynchronous orbit: Hot plasma, cold plasma, and the solar wind, *J. Geophys. Res.*, *113*, A07216, doi:10.1029/2007JA012998.

Denton, M. H., and J. E. Borovsky (2008b), The superdense plasma sheet in the magnetosphere during high-speed-stream driven storms: Plasma transport timescales, *J. Atmos. Solar. Terr. Phys.*, in press.

Denton, M. H., M. F. Thomsen, H. Korth, S. Lynch, J. C. Zhang, and M. W. Liemohn (2005), Bulk plasma properties at geosynchronous orbit, *J. Geophys. Res.*, *110*, A07223, doi:10.1029/2004JA010861.

Denton, M. H., J. E. Borovsky, R. M. Skoug, M. F. Thomsen, B. Lavraud, M. G. Henderson, R. L. McPherron, J. C. Zhang, and M. W. Liemohn (2006), Geomagnetic storms driven by ICME- and CIR-dominated solar wind, *J. Geophys. Res.*, *111*, A07S07, doi:10.1029/2005JA011436.

Denton, M. H., J. E. Borovsky, R. B. Horne, R. L. McPherron, S. K. Morley, and B. T. Tsurutani (2008), High-speed solar wind streams: A call for key research, *EOS Trans. Am. Geophys. Soc.*, *89*, 62.

Desorgher, L., E. Fluckiger, P. Buhler, and A. Zehnder (2000), Modelling of the outer electron belt flux dropout and losses during magnetic storm main phase, *Adv. Space Res.*, *26*, 167.

Dessler, A. J., and R. Karplus (1961), Some effects of diamagnetic ring currents on Van Allen radiation, *J. Geophys. Res.*, *66*, 2289.

Ebihara, Y., and M. Ejiri (2000), Simulation study on fundamental properties of the storm-time ring current, *J. Geophys. Res.*, *105*, 15,843.

Ebihara, Y., and M. Ejiri (2002), Numerical simulation of the ring current: Review, *Space Sci. Rev.*, *105*, 377.

Ebihara, Y., M. C. Fok, R. A. Wolf, M. F. Thomsen, and T. E. Moore (2005), Nonlinear impact of plasma sheet density on the storm-time ring current, *J. Geophys. Res.*, *110*, A02208, doi:10.1029/2004JA010435.

Ejiri, M., R. A. Hoffman, and P. H. Smith (1980), Energetic particle penetrations into the inner magnetosphere, *J. Geophys. Res.*, *85*, 653.

Elphic, R. C., L. A. Weiss, M. F. Thomsen, D. J. McComas, and M. B. Moldwin (1996), Evolution of plasmaspheric ions at geosynchronous orbit during times of high geomagnetic activity, *Geophys. Res. Lett.*, *23*, 2189.

Elphic, R. C., M. F. Thomsen, J. E. Borovsky, and D. J. McComas (1999), Inner edge of the electron plasma sheet: Empiracal models of boundary location, *J. Geophys. Res.*, *104*, 22,679.

Erickson, K. N., and J. R. Winckler (1973), Auroral electroets and evening sector electron dropouts at synchronous orbit, *J. Geophys. Res.*, *78*, 8373.

Fraser, B. J., and T. S. Nguyen (2001), Is the plasmapause a preferred source region of electromagnetic ion cyclotron waves in the magnetoshere?, *J. Atmos. Solar Terr. Phys.*, *63*, 1225.

Fraser, B. J., T. M. Loto'aniu, and H. J. Singer (2006). Electromagnetic ion cyclotron waves in the magnetosphere, in *Magnetospheric ULF Waves*, edited by K. Takahashi et al., p. 195, AGU, Washington, D. C.

Freeman, J. W. (1964), The morphology of the electron distribution in the outer radiation zone and near the magnetospheric boundary as observed by Explorer 12, *J. Geophys. Res.*, *69*, 1691.

Friedel, R. H. W., G. D. Reeves, and T. Obara (2002), Relativistic electron dynamics in the inner magnetophere—A review, *J. Atmos. Solar Terr. Phys.*, *64*, 265.

Fujimoto, M., T. Mukai, A. Matsuoka, Y. Saito, H. Hayakawa, S. Kokubun, and R. P. Lepping (2000), Multi-point observations of cold-dense plasma sheet and its relation with tail-LLBL, *Adv. Space Res.*, *25*, 1607.

Fujimoto, M., T. Mukai, and S. Kokubun (2002), Cold-dense plasma sheet and hot-dense ions in the inner-magnetosphere, *Adv. Space Res.*, *30*, 2279.

Fujimoto, M., T. Mukai, and S. Kokubun (2005), The structure of the plasma sheet under northward IMF, in *Frontiers in Magnetospheric Plasma Physics*, edited by M. Hoshino, Y. Omura, and L. J. Lanzerotti, p. 19, Elsevier, Amsterdam.

Fuselier, S. A., S. P. Gary, M. F. Thomsen, E. S. Claflin, B. Hubert, B. R. Sandel, and T. Immel (2004), Generation of transient dayside subauroral proton precipitation, *J. Geophys. Res.*, *109*, A12227, doi:10.1029/2004JA010393.

Goldstein, J., B. R. Sandel, M. F. Thonsen, M. Spasojevic, and P. H. Reiff (2004), Simultaneous remote sensing and in situ observations of plasmaspheric drainage plumes, *J. Geophys. Res.*, *109*, A03202, doi:10.1029/2003JA010281.

Gosling, J. T., J. R. Asbridge, S. J. Bame, and W. C. Feldman (1978), Solar wind stream interfaces, *J. Geophys. Res.*, *83*, 1401.

Green, J. C., T. G. Onsager, T. P. O'Brien, and D. N. Baker (2004), Testing loss mechanisms capable of rapidly depleting relativistic electron flux in the Earth's outer radiation belt, *J. Geophys. Res.*, *109*, A12211, doi:10.1029/2004JA010579.

Greenspan, M. E., D. J. Williams, B. H. Mauk, and C.-I. Meng (1985), Ion and electron energy dispersion featerues detected by ISEE 1, *J. Geophys. Res.*, *90*, 4079.

Gussenhoven, M. S., D. A. Hardy, and N. Heinemann (1983), Systematics of the equatorward diffuse auroral boundary, *J. Geophys. Res.*, *88*, 5692.

Higel, B., and W. Lei (1984), Electron density and plasmapause characteristics at 6.6 Re: A statistical study of GEOS 2 relaxation sounder data, *J. Geophys. Res.*, *89*, 1583.

Horne, R. B., and R. M. Thorne (1998), Potential waves for relativistic electron scattering and stochastic acceleration during magnetic storms, *Geophys. Res. Lett.*, *25*, 3011.

Horne, R. B., N. P. Meredith, R. M. Thorne, D. Heynderickx, R. H. A. Iles, and R. R. Anderson (2003), Evolution of energetic electron pitch angle distributions during storm time electron acceleration to megaelectronvolt energies, *J. Geophys. Res.*, *108*(A1), 1016, doi:10.1029/2001JA009165.

Horwitz, J. L., S. Menteer, J. Turnley, J. L. Burch, J. D. Winningham, C. R. Chappell, J. D. Craven, L. A. Frank, and D. W. Slater (1986), Plasma boundaries in the inner magnetosphere, *J. Geophys. Res.*, *91*, 8861.

Hundhausen, A. J. (1973), Nonlinear model of high-speed solar wind streams, *J. Geophys. Res.*, *78*, 1528.

Iles, R. H. A., A. N. Fazkerley, A. D. Johnstone, N. P. Meredith, and P. Buhler (2002), The relativistic electron response in the outer radiation belt during magnertic storms, *Ann. Geophys.*, *20*, 957.

Jordanova, V. K., C. J. Farrugia, J. M. Quinn, R. B. Torbert, J. E. Borovsky, R. B. Sheldon, and W. K. Peterson (1999), Simulation of off-equatorial ring current ion spectra measured by Polar for moderate storm at solar minimum, *J. Geophys. Res.*, *104*, 429.

Jordanova, V. K., Y. S. Miyoshi, S. Zaharia, M. F. Thomsen, G. D. Reeves, D. S. Evans, C. G. Mouikis, and J. F. Fennell (2006), Kinetic simulations of ring current evolution during the Geospace Environment Modeling challenge events, *J. Geophys. Res.*, *111*, A11S10, doi:10.1029/2006JA011644.

Jordanova, V. K., M. Spasojevic, and M. F. Thomsen (2007), Modeling the electromagnetic ion cyclotron wave-induced formation of detached subauroral proton arcs, *J. Geophys. Res.*, *112*, A08209, doi:10.1029/2006JA012215.

Kavanagh, A. J., and M. H. Denton (2007), High-speed solar-wind streams and geospace interactions, *Aston. Geophys.*, *48*, 6.24.

Kaye, S. M., M. G. Kivelson, and D. J. Southwood (1979), Evolution of ion cyclotron instability in the plasma convection system of the magnetosphere, *J. Geophys. Res.*, *84*, 6397.

Khazanov, G. V., K. V. Gamayunov, D. L. Gallagher, and J. U. Kozyra (2006), Self-consistent model of magnetospheric ring current and propagating electromagnetic ion cyclotron waves: Wwaves in multi-ion magnetosphere, *J. Geophys. Res.*, *111*, A10202, doi:10.1029/2006JA011833.

Kim, H.-J., and A. A. Chan (1997), Fully adiabatic changes in storm time relativistic electron fluxes, *J. Geophys. Res.*, *102*, 22,107.

King, J. H., and N. E. Papitashvili (2005), Solar wind spatial scales in and comparisons of hourly Wind and ACE plasma and magnetic field data, *J. Geophys. Res.*, *110*, A02104, doi:10.1029/2004JA010649.

Kistler, L. M., F. M. Ipavich, D. C. Hamilton, G. Gloeckler, B. Wilken, G. Kremser, and W. Studemann (1989), Energy spectra of the major ion species in the ring current during geomagnetic storms, *J. Geophys. Res.*, *94*, 3579.

Kistler, L. M., et al. (1999), Tesing electric field models using ring current ion energy spectra from the Equator-S ion composition (ESIC) instrument, *Ann. Geophys.*, *17*, 1611.

Knipp, D. J., et al. (1998), An overview of the early November 1993 geomagnetic storm, *J. Geophys. Res.*, *103*, 26197.

Korth, H., M. F. Thomsen, J. E. Borovsky, and D. J. McComas (1999), Plasma sheet access to geosynchronous orbit, *J. Geophys. Res.*, *104*, 25,047.

Korth, H., M. F. Thomsen, K.-H. Glassmeier, and W. S. Phillips (2002), Particle tomography of the inner magnetosphere, *J. Geophys. Res.*, *107* (A9), 1229, doi:10.1029/2001JA000147.

Kovalevskiy, I. V. (1980), Ion-cyclotron instability in the frontal boundary layer of the geomagnetosphere produced by detached plasma clouds, *Geomag. Aeron.*, *20*, 338.

Kovalevskiy, I. V. (1981), Cyclotron instability during interaction of detached plasma regions with the plasma sheet during substorms, *Geomag. Aeron.*, *21*, 83.

Kozyra, J. U., and M. W. Liemohn (2003), Ring current energy input and decay, *Space Sci. Rev.*, *109*, 105.

Kozyra, J. U., V. K. Jordanova, J. E. Borovsky, M. F. Thomsen, D. J. Knipp, D. S. Evans, D. J. McComas, and T. E. Cayton (1998), Effects of a high-density plasma sheet on ring current development during the November 2–6, 1993 magnetic storm, *J. Geophys. Res.*, *103*, 26,285.

Lam, H.-L. (2004), On the prediction of relativistic electron fluence based on its relationship with geomagnetic activity over a solar cycle, *J. Atmos. Solar-Terr. Phys.*, *66*, 1703.

Lavraud, B., and V. K. Jordanova (2007), Modeling the effects of cold-dense and hot-tenuous plasma sheet on proton ring current energy and peak location, *Geophys. Res. Lett.*, *34*, L02102, doi:10.1029/2006GL027566.

Lavraud, B., M. H. Denton, M. F. Thomsen, J. E. Borovsky, and R. H. W. Friedel (2005), Superposed epoch analysis of dense plasma access to geosynchronous orbit, *Ann. Geophys.*, *23*, 2519.

Lavraud, B., M. F. Thomsen, J. E. Borovsky, M. H. Denton, and T. I. Pulkkinen (2006), Magnetosphere preconditioning under northward IMF: Evidence from the study of coronal mass ejection and corotating interaction region geoeffectiveness, *J. Geophys. Res.*, *111*, A09208, doi:10.1029/2005JA011566.

Li, X., D. N. Baker, M. Temerin, T. E. Cayton, E. G. D. Reeves, R. A. Christensen, J. B. Blake, M. D. Looper, R. Nakamura, and S. G. Kanekal (1997), Multispacecraft observations of the outer zone electron variation during the November 3–4, 1993, magnetic storm, *J. Geophys. Res.*, *102*, 14,123.

Liemohn, M. W., J. U. Kozyra, V. K. Jordanova, G. V. Khazanov, M. F. Thomsen, and T. E. Cayton (1999), Analysis of early phase ring current recovery mechanisms during geomagnetic storms, *Geophys. Res. Lett.*, *26*, 2845.

Longden, N., M. H. Denton, and F. Honary (2008), Particle precipitation during ICME-driven and CIR-driven geomagnetic storms, *J. Geophys. Res.*, *113*, A06205, doi:10.1029/2007JA012752.

Love, D. L., D. S. Toomb, D. C. Wilkinson, and J. B. Parkinson (2000), Penetrating electron fluctuations associated with GEO spacecraft anomalies, *IEEE Trans. Plasma Sci.*, *28*, 2075.

Mathie, R. A., and I. R. Mann (2000), A correlation between extended intervals of ULF wave power and storm-time geosynchronous relativistic electron flux enhancements, *Geophys. Res. Lett.*, *27*, 3261.

Mauk, B. H., and C. I. Meng (1983), Dynamical injections as the source of near geostationary quiet time particle spatial boundaries, *J. Geophys. Res.*, *88*, 10,011.

Maurice, S., M. F. Thomsen, D. J. McComas, and R. C. Elphic (1998), Quiet time densities of hot ions at geosynchronous orbit, *J. Geophys. Res.*, *103*, 17,571.

McPherron, R. L., and J. Weygand (2006), The solar wind and geomagnetic activity as a function of time relative to corotating interaction regions, in *Recurrent Magnetic Storms*, edited by B. Tsurutani et al., p. 125, AGU, Washington, D. C.

Meredith, N. P., R. M. Thorne, R. B. Horne, D. Summers, B. J. Fraser, and R. R. Anderson (2003), Statistical analysis of relativistic electron energies for cyclotron resonance with EMIC waves observed on CRRES, *J. Geophys. Res.*, *108*(A6), 1250, doi:10.1029/2002JA009700.

Meredith, N. P., R. B. Horne, R. M. Thorne, D. Summers, and R. R. Anderson (2004), Substorm dependence of plasmaspheric hiss, *J. Geophys. Res.*, *109*, A06209, doi:10.1029/2004JA010387.

Meredith, N. P., R. B. Horne, S. A. Glauert, R. M. Thorne, D. Summers, J. M. Albert, and R. R. Anderson (2006), Energetic outer zone electron loss timescales during low geomagnetic activity, *J. Geophys. Res.*, *111*, A05212, doi:10.1029/2005JA011516.

Miyoshi, Y., and R. Kataoka (2005), Ring current ions and radiation belt electrons during geomagnetic storms driven by coronal mass ejections and corotating interaction regions, *Geophys. Res. Lett.*, *32*, L21105, doi:10.1029/2005GL024590.

Moldwin, M. B., M. F. Thomsen, S. J. Bame, and D. McComas (1995), The fine-scale structure of the outer plasmasphere, *J. Geophys. Res.*, *100*, 8021.

Moldwin, M. B., J. Howard, J. Sanny, J. D. Bocchicchio, H. Rassoul, and K. Anderson (2004), Plasmaspheric plumes: CRRES observations of enhanced density beyond the plasmapause, *J. Geophys. Res.*, *109*, A05202, doi:10.1029/2003JA010320.

Mursula, K., and B. Zeiger (1996), The 13.5-day periodicity in the sun, solar wind, and geomagnetic activity: The last three solar cycles, *J. Geophys. Res.*, *101*, 27,077.

Nagai, T. (1988), "Space weather forecast" prediction of relativistic electron intensity at synchronous orbit, *Geophys. Res. Lett.*, *15*, 425.

Neugebauer, M., P. C. Liewer, B. E. Goldstein, X. Zhou, and J. T. Steinberg (2004), Solar wind stream interaction regions without sector boundaries, *J. Geophys. Res.*, *109*, A10102, doi:10.1029/2004JA010456.

Nishino, M. N., T. Terasawa, and M. Hoshino (2002), Increase of the tail plasma content during the northward interplanetary magnetic field intervals: Case studies, *J. Geophys. Res.*, *107*(A9), 1261, doi:10.1029/2002JA009268.

Onsager, T. G., G. Rostoker, H.-J. Kim, G. D. Reeves, T. Obara, H. J. Singer, and C. Smithtro (2002), Radiation belt electron flux dropouts: Local time, radial, and particle-energy dependence, *J. Geophys. Res.*, *107*(A11), 1382, doi:10.1029/2001JA000187.

Onsager, T. G., J. C. Green G. D. Reeves, and H. J. Singer (2007), Solar wind and magnetospheric conditions leading to the abrupt loss of outer radiation belt electrons, *J. Geophys. Res.*, *112*, A01202, doi:10.1029/2006JA011708.

Paulikas, G. A., and J. B. Blake (1976), Modulation of trapped energetic electrons at 6.6 Re by the interplanetary magnetic field, *Geophys. Res. Lett.*, *3*, 277.

Phan, T. D., R. P. Lin, S. A. Fuselier, and M. Fujimoto (2000), Wind observations of mixed magnetosheath-plasma sheet ions deep inside the magnetosphere, *J. Geophys. Res.*, *105*, 5497.

Reeves, G. D. (1998), Relativistic electrons and magnetic storms: 1992–1995, *Geophys. Res. Lett.*, *25*, 1817.

Richardson, I. G., G. Wibberenz, and H. V. Cane (1996), The relationship between recurring cosmic ray depressions and corotating solar wind streams at 1 AU: IMP 8 and Helios 1 and 2 anticoincidence guard rate observations, *J. Geophys. Res.*, *101*, 13,483.

Richter, A. K., and A. H. Luttrell (1986), Superposed epoch analysis of corotating interaction regions at 0.3 and 1.0 AU: A comparitive study, *J. Geophys. Res.*, *91*, 5873.

Rostoker, G., S. Skone, and D. N. Baker (1998), On the origin of relativistic electrons in the magnetosphere associated with some geomagnetic storms, *Geophys. Res. Lett.*, *25*, 3701.

Russell, C. T., and R. L. McPherron (1973), Semiannual variation of geomagnetic activity, *J. Geophys. Res.*, *78*, 92.

Sandanger, M., F. Sørass, K. Aarsnes, K. Oksavik, and D. S. Evans (2007), Loss of relativistic electrons: Evidence for pitch angle scattering by electromagnetic ion cyclotron waves excited by unstable ring current protons, *J. Geophys. Res.*, *112*, A12213, doi:10.1029/2006JA012138.

Sauvaud, J. A., and J. R. Winckler (1980), Dynamics of plasma, energetic particles, and fields near synchronous orbit in the nighttime sector during magnetospheric substorms, *J. Geophys. Res.*, *85*, 2043.

Sauvaud, J. A., T. Beutier, and D. Delcourt (1996), On the origin of flux dropouts near geosynchronous orbit during the growth phase of substorms: 1 Betatron effects, *J. Geophys. Res.*, *101*, 19,911.

Sckopke, N. (1966), A general relation between the energy of trapped particles and the disturbance field near the earth, *J. Geophys. Res.*, *71*, 3125.

Shprits, Y. Y., R. M. Thorne, R. Friedel, G. D. Reeves, J. Fennell, D. N. Baker, and S. G. Kanekal (2006), Outward radial diffusion driven by losses at magnetopause, *J. Geophys. Res.*, *111*, A11214, doi:10.1029/2006JA011657.

Siscoe, G. L., B. Goldstein, and A. J. Lazarus (1969), An east-west asymmetry in the solar wind velocity, *J. Geophys. Res.*, *74*, 1759.

Smith, A. J., R. B. Horne, and N. P. Meredith (2004), Ground observations of chorus following geomagnetic storms, *J. Geophys. Res.*, *109*, A02205, doi:10.1029/2003JA010204.

Sojka, J. J., and G. L. Wrenn (1985), Refilling of geosynchronous flux tubes as observed at the equator by GEOS 2, *J. Geophys. Res.*, *90*, 6379.

Solomon, J., and O. Picon (1981), Charge exchange and wave-particle interaction in the proton ring current, *J. Geophys. Res.*, *86*, 3335.

Spasojevic, M., J. Goldstein, D. L. Carpenter, U. S. Inan, B. R. Sandel, M. B. Moldwin, and B. W. Reinisch (2003), Global response of the plasmasphere to a geomagnetic disturbance, *J. Geophys. Res.*, *198*(A9), 1340, doi:10.1029/2003JA009987.

Spasojevic, M., H. U. Frey, M. F. Thomsen, S. A. Fuselier, S. P. Gary, B. R. Sandel, and U. S. Inan (2004), The link between a detached subauroral proton arc and a plasmaspheric plume, *Geophys. Res. Lett.*, *31*, L04803, doi:10.1029/2003GL018389.

Spiro, R. W., M. Harel, R. A. Wolf, and P. H. Reiff (1981), Quantitative simulation of a magnetospheric substorm: 3. Plasmaspheric electric fields and evolution of the plasmapause, *J. Geophys. Res.*, *86*, 2261.

Su, Y.-J., J. E. Borovsky, M. F. Thomsen, R. C. Elphic, and D. J. McComas (2000), Plasmaspheric material at the reconnecting magnetopause, *J. Geophys. Res.*, *105*, 7591.

Su, Y.-J., M. F. Thomsen, J. E. Borovsky, and D. J. Lawrence (2001), A comprehensive survey of plasmasphere refilling at geosynchronous orbit, *J. Geophys. Res.*, *106*, 25,615.

Summers, D., and R. M. Thorne (2003), Relativistic electron pitch-angle scattering by electromagnetic ion cyclotron waves during geomagnetic storms, *J. Geophys. Res.*, *108*(A4), 1143, doi:10.1029/2002JA009489.

Summers, D., R. M. Thorne, and F. L. Xiao (1998), Relativistic theory of wave-particle resonant diffusion with application to electron acceleration in the magnetosphere, *J. Geophys. Res.*, *103*, 20,487.

Summers, D., C. Ma, N. P. Meredith, R. B. Horne, R. M. Thorne, and R. R. Anderson (2004), Modeling outer-zone relativistic electron response to whistler-mode chorus activity during substorms, *J. Atmos. Sol. Terr. Phys.*, *66*, 133.

Taylor, H. A., H. C. Brinton, and A. R. Deshmukh (1970), Observations of irregular structure in thermal ion distributions in the duskside magnetosphere, *J. Geophys. Res.*, *75*, 2481.

Thomsen, M. F. (2004), Why Kp is such a good measure of magnetospheric convection, *Space Weather*, *2*, S11004, doi:10.1029/2004SW000089.

Thomsen, M. F., S. J. Bame, D. J. McComas, M. B. Moldwin, and K. R. Moore (1994), The magnetospheric lobe at geosynchronous orbit, *J. Geophys. Res.*, *99*, 17,283.

Thomsen, M. F., J. E. Borovsky, D. J. McComas, and M. B. Moldwin (1996), Observations of the Earth's plasma sheet at geosynchronous orbit, in *Workshop on the Earth's Trapped Particle Environment, AIP Conference Proceedings 383*, edited by G. D. Reeves, p. 25, American Institute of Physics, New York.

Thomsen, M. F., J. E. Borovsky, D. J. McComas, and M. R. Collier (1998a), Variability of the ring current source population, *Geophys. Res. Lett.*, *25*, 3481.

Thomsen, M. F., D. J. McComas, J. E. Borovsky, and R. C. Elphic (1998b), The magnetospheric trough, in *Geospace Mass Transport and Energy Flow: Results From the International Solar-Terrestrial Physics Program*, edited by J. L. Horwitz, D. L. Gallagher, and W. K. Peterson, p. 355, AGU, Washington, D. C.

Thomsen, M. F., J. E. Borovsky, R. M. Skoug, and C. W. Smith (2003), Delivery of cold, dense plasma sheet material into the near-Earth region, *J. Geophys. Res.*, *108*(A4), 1151, doi:10.1029/2002JA009544.

Thorne, R. B., and C. F. Kennel (1971), Relativistic electron precipitation during magnetic storm main phase, *J. Geophys. Res.*, *76*, 4446.

Thorne, R. M., and R. B. Horne (1997), Modulation of electromagnetic ion cyclotron instability duro to interaction with ring current O^+ during magnetic storms, *J. Geophys. Res.*, *102*, 14,155.

Thorne, R. M., S. R. Church, and D. J. Gorney (1979), On the origin of plasmaspheric hiss: The importance of wave propagation and the plasmapause, *J. Geophys. Res.*, *84*, 5241.

Thorne, R. M., R. B. Horne, V. K. Jordanova, J. Bortnik, and S. Glauert (2006), Interaction of EMIC waves with thermal plasma and radiation belt particles, in *Magnetospheric ULF Waves*, edited by K. Takahashi et al., p. 213, AGU, Washington, D. C.

Tsurutani, B. T., and E. J. Smith (1974), Postmidnight chorus: A substorm phenomenon, *J. Geophys. Res.*, *79*, 118.

Tsurutani, B. T., and E. J. Smith (1977), Two types of ELF chorus and their substorm dependences, *J. Geophys. Res.*, *82*, 5112.

Tsurutani, B., R. McPherron, W. Gonzalez, G. Lu, J. H. A. Sobral, and N. Gopalswamy (Eds.) (2006a), *Recurrent Magnetic Storms: Corotating Solar Wind Streams*, AGU, Washington, D. C.

Tsurutani, B. T., et al. (2006b), Corotating solar wind streams and recurrent geomagnetic activity: A review, *J. Geophys. Res.*, *111*, A07S01, doi:10.1029/2005JA011273.

Turner, N. E., E. J. Mitchell, D. J. Knipp, and B. A. Emery (2006), Energetics of magnetic storms driven by corotating interaction regions: A study of

geoeffectiveness, in *Recurrent Magnetic Storms*, edited by B. Tsurutani et al., p. 113, AGU, Washington, D. C.

West, H. I., R. M. Buck, and J. R. Walton (1972), Shadowing of electron azimuthal-drift motions near the noon magnetopause, *Nature Phys. Sci.*, *240*, 6.

Yahnin, A. G., and T. A. Yahnina (2007), Energetic proton precipitation related to ion-cyclotron waves, *J. Atmos. Solar Terr. Phys.*, *69*, 1690.

Yermolaev, Y. U., and M. Y. Yermolaev (2002), Statistical relationships between solar, interplanetary, and geomagnetospheric disturbances, 1976–2000, *Cosmic Res.*, *40*, 1.

Yermolaev, Y. I., M. Y. Yermolaev, I. G. Lodkina, and N. S. Nikolaeva (2007), Statistical investigation of heliospheric conditions resulting in magnetic storms, *Cosmic Res.*, *45*, 1.

Zhang, J. C., M. W. Liemohn, J. U. Kozyra, M. F. Thomsen, H. A. Elliott, and J. M. Weygand (2006), A statistical comparison of solar wind sources of moderate and intense geomagnetic storms at solar minimum and maximum, *J. Geophys. Res.*, *11*, A01104, doi:10.1029/2005JA011065.

J. E. Borovsky, Space Science and Applications (ISR-1), Los Alamos National Laboratory, Mail Stop D466, Los Alamos, NM 87545, USA. (jborovsky@lanl.gov)

M. H. Denton, Space Plasma Environment and Radio Science, Department of Communication Systems, Lancaster University, Lancaster LA1 4WA, UK.